# Hydrological contaminant mobilisation from thawing permafrost in Alaska

Daniëlle Kraak[1,2,*], Jan Nitzbon[2,3], Simone Stuenzi[2,4], Soraya Kaiser[2], Alexander Oehme[2], Christina Himmelsbach[2,4], Pernille Erland Jensen[5], Sebastian Westermann[6,7], Jorien E. Vonk[1], Moritz Langer[1,2]

[1] Department of Earth Sciences, Faculty of Science, Vrije Universiteit Amsterdam, Amsterdam, The Netherlands
[2] Alfred Wegener Institute, Helmholtz Centre for Polar and Marine Research, Potsdam, Germany
[3] Institute for Geography, University of Göttingen, Göttingen, Germany
[4] Geography Department, Humboldt-Universität zu Berlin, Berlin, Germany
[5] Arctic Technology Centre, Department of Civil Engineering, Technical University of Denmark, Kongens Lyngby, Denmark
[6] Department of Geosciences, University of Oslo, Oslo, Norway
[7] Centre for Biogeochemistry in the Anthropocene, University of Oslo, Oslo, Norway

**Corresponding author**
Daniëlle Kraak
Email: d.kraak@vu.nl

# Hydrological contaminant mobilisation from thawing permafrost in Alaska

Daniëlle Kraak*[1,2], Jan Nitzbon[2,3] Simone Stuenzi[4,2] Soraya Kaiser[2], Alexander Oehme[2], Christina Himmelsbach[2,4] Pernille Erland Jensen[5], Sebastian Westermann[6,7], Jorien E. Vonk[1], Moritz Langer[1,2]

**1** Department of Earth Sciences, Faculty of Science, Vrije Universiteit Amsterdam, Amsterdam, Netherlands
**2** Helmholtz Centre for Polar and Marine Research, Alfred Wegener Institute, Potsdam, Germany
**3** Institute for Geography, University of Göttingen, Göttingen, Germany
**4** Geography Department, Humboldt-Universität zu Berlin, Berlin, Germany
**5** Arctic Technology Centre, Department of Civil Engineering, Technical University of Denmark, Kongens Lyngby, Denmark
**6** Department of Geosciences, University of Oslo, Norway
**7** Centre for Biogeochemistry in the Anthropocene, University of Oslo, Norway

* d.kraak@vu.nl

## Abstract

Global warming and permafrost thaw increasingly threaten contaminated sites across Alaska, altering contaminant mobilisation risks in sensitive ecosystems and communities. To assess this threat, we used the SIRIUS database to identify 1261 active contaminated sites within Alaska's permafrost region, noting that many sit near lakes, rivers, and coastlines. We evaluated current and future hydrological mobilisation potential at these sites using the CryoGridLite model under SSP1-2.6 and SSP5-8.5 climate scenarios, accounting for how permafrost thaw and shifting precipitation alter groundwater levels. We then determined overall aquatic hazard potential by integrating site-specific characteristics, including contaminant toxicity, solubility, and proximity to water bodies. Our results show that across Alaska 428 contaminated sites already carry a 'high' to 'very high' mobilisation risk. In the Alaska Tundra ecoregion, about 48% (238) of contaminated sites fall into these categories, while the Alaska Boreal Interior (110 sites, 9.6%) and Boreal Cordillera ecoregions (36 sites, 29.3%) contain fewer high-risk sites and show limited future change. These regional differences reflect distinct environmental controls: in tundra regions, proximity to water bodies and extensive wetland networks heighten mobilisation potential despite generally lower contaminant toxicity, whereas higher contaminant toxicity dominates the drier Boreal Interior where hydrological pathways are limited. While northern coastal regions show the largest relative increases in hydrological mobilisation potential, absolute values remain low, causing minor changes in risk classification. Conversely, drying in central Alaska, likely driven by increased evapotranspiration, could reduce future contaminant mobilisation potential despite enhanced permafrost thaw. Ultimately, these findings highlight the complex and regionally distinct controls on contaminant mobilisation under climate change, offering crucial guidance for targeted northern environmental management.

## Author summary

Permanently frozen ground has historically limited soil water movement in the vicinity of contaminated sites across Alaska. Rising temperatures in the Arctic cause permafrost thaw and contaminants stored at these sites could become more mobile, potentially polluting nearby lakes, rivers, coastal waters, ecosystems and communities. In this study, we assessed the risk of contaminant mobilisation for over 1200 active contaminated sites across Alaska's permafrost regions. We combined information on contaminant characteristics, such as toxicity and solubility, with distance to the nearest WBs and hydrological simulations under future climate scenarios. Our results show that many sites in the Alaska tundra region already have a high potential for contaminant mobilisation, which would further increase under strong warming scenarios. However, boreal regions show lower increases because their drier conditions could reduce water-driven mobilisation despite ongoing thaw. Our findings show that climate change could influence contaminant mobilisation risk in different ways across Alaska and highlight the importance of considering local environmental conditions when prioritising monitoring and remediation efforts.

# Introduction

Global warming is leading to substantial changes in the hydrological connectivity of Arctic permafrost landscapes [1–4], with implications for a range of processes, including the potential spread and mobilisation of contaminants [5]. Historically, the presence of permafrost has limited both vertical and lateral movement of contaminants through groundwater [6–8]. Climate warming, however, is altering the thermohydrological conditions of the ground, reducing the integrity of permafrost as a hydrological barrier and potentially increasing the risk of contaminant mobilisation.

Key processes driving changes in hydrological connectivity associated with permafrost degradation include active-layer deepening, the formation of taliks and thermokarst development in ice-rich permafrost [9–13]. In ice-rich polygonal tundra, melting of ice wedges can rapidly create new hydrological pathways as polygonal troughs become interconnected [4]. These changes can occur over relatively short timescales of only a few decades [3]. Lake drainage is another process indicative of an increasing connectivity [14]. For example, the Seward Peninsula and Baldwin Peninsula experienced substantial lake area losses in 2018 [15]. In addition, thinning lake ice can promote talik formation beneath lakes, increasing lateral seepage [15] which can lead to a decline in discontinuous and sporadic permafrost regions [2, 10, 12]. Hydrological connectivity is further influenced by changes in precipitation and runoff regimes. Precipitation is projected to increase across much of the Arctic, accompanied by a transition from snowmelt-dominated to increasingly rainfall-driven runoff in Arctic rivers [16, 17].

In combination with permafrost thaw, these shifts enhance hydrological connectivity and increase the potential for dissolved or particulate substances to be transported across landscapes [18]. Pringle [19] noted that the Arctic food chain and water supply contain substantial amounts of Polychlorinated Bisphenyls (PCBs) due to increases in hydrological connectivity. This was also found by Adams et al., [20] who detected increased PCBs levels in mussels and salmon close to former military bases in the Aleutian arc.

At the same time, the Arctic contains a large number of contaminated sites, resulting from decades of human activity, including industrial operations, oil and gas exploration, military installations and waste disposal practices [5, 21–26]. These activities have introduced a wide range of contaminants into permafrost soils. Langer et al., [5] estimate that between 10,000 and 20,000 contaminated sites related to industrial activities are located within the Arctic permafrost region. Due to the remote locations for a lot of these sites, cleaning them up is costly and difficult. Remains of human and industrial activities in the Arctic are therefore typically not cleaned out or removed to the extent that is the case for mid-latitude regions [5, 7].

While site-specific studies have investigated contaminant behaviour and mobilisation at individual locations in the Arctic permafrost-affected environments - including reactive solute transport modelling in groundwater systems and contaminant measurements in thawing catchments and river systems [27–29] - the implications of permafrost thaw for contaminant mobilisation remain poorly constrained at larger regional scales. Existing studies primarily assess environmental and economic risks associated with permafrost-related infrastructure failure (e.g. [30–35]) and are not necessarily related to contamination. These studies demonstrate the value of large-scale risk assessments under different climate change scenarios, but typically focus on infrastructure stability (e.g. housing, pipelines, waste disposal sites) rather than the mobilisation potential of contaminants stored at contaminated sites.

Aquatic contaminant release as a human health hazard is understudied in the Arctic, which could be problematic due to the proximity of many contaminated sites to settlements. Approximately 5 million people live in Arctic permafrost regions across 1000 settlements [36]. Since 2000, human-impacted areas along Arctic coastlines have expanded by 15%, largely due to oil and gas exploration and processing [25]. In some regions, contamination has already led communities to restrict access to traditionally used lands [37, 38] and to restrictions and/or cautions to use traditional drinking water sources such as rivers and lakes (e.g. [39–41]). Regional-scale risk assessments are therefore needed to identify potentially vulnerable sites and to support prioritisation for monitoring and remediation efforts at these sites.

To address this gap, we combine a database of contaminated sites with information on contaminant toxicity and solubility with numerical modeling of the hydrological mobilization potential under current and future climate conditions. We assess the aquatic hazard potential of contaminated sites across Alaska's permafrost regions and evaluate how permafrost thaw and changing hydrological connectivity could alter contaminant mobilisation risk under SSP1-2.6 and SSP5-8.5 climate scenarios. Specifically, we identify where contaminated sites are most vulnerable to hydrological mobilisation and examine how these risks vary across Alaska's ecoregions. By providing a first-order assessment of contaminant mobilisation potential, this study supports the prioritisation of sites for monitoring, remediation, and detailed local risk assessments by agencies and communities facing increasing environmental change.

# Study region

Alaska is a geographically and environmentally diverse region, characterised by strong variations in topography, climate, hydrology and permafrost conditions. This diversity plays a fundamental role in the distribution of contaminated sites and their potential for contaminant mobilisation.

Alaska contains several large mountain ranges, including the Brooks Range in the north and the Aleutian range in the south-west. The Brooks Range forms an east-west barrier separating the Arctic coastal plain from the interior.

With over 3 million lakes and over 12,000 rivers, streams and creeks, Alaska has an extensive freshwater network. The Yukon river is the largest river and drains about two-thirds of the state into the Bering Sea [42]. Glaciation is most extensive in the southern mountain ranges, with smaller glacier coverage in the Brooks Range [43].

Alaska is underlain by extensive permafrost, ranging from continuous permafrost in the north, to discontinuous, sporadic and isolated patches toward the south [44]. The continuous permafrost zone extends south of the Brooks Range, before transitioning into discontinuous permafrost across most of the interior and western coastline. Sporadic permafrost occurs along the margins of the discontinuous zone, while isolated patches are mainly found along the southern edges of the boreal interior and coastal regions near the Yukon Delta [44].

Due to the topographical, climatological and biological diversity, Alaska is divided into several ecoregions. In this study, we use the Level II ecoregions defined by the CEC [45] to place contaminant release in a regional context and distinguish differences in vulnerability of contaminated sites.

The Alaska Tundra, the northernmost ecoregion, consists of lowland plains and mountainous terrain with long, dark and cold winters (-31 to -17°C) and short, cool summers (1.5 to 6°C) with extensive daylight. Mean annual temperatures range from -17°C in the north, to -7°C in the south. Despite low annual precipitation (100-500 mm), the region contains abundant lakes, ponds and wetlands and has shallow Active Layers [43, 45]).

The Brooks Range Tundra is more mountainous and slightly wetter (200-600 mm annually), with mean annual temperatures between -6 to -12°C, depending strongly on elevation. Drainage mainly occurs through deep, incised river valleys, with few large lakes [43].

The Alaska Boreal Interior covers much of interior Alaska and has a subarctic, continental climate, with mean annual temperatures between -9.5 and -4°C and precipitation of 200 to 800 mm. Wetlands are less common, but thaw ponds and oxbow lakes are widespread. Permafrost is predominantly discontinuous and contributes to poor drainage and wet, organic-rich soils [43].

The Boreal Cordillera and Marine West Coast Forest are more mountainous and wetter, with stronger marine influences in the south. These regions experience higher precipitation (up to ¿3000 mm) and generally warmer conditions, with discontinuous to completely absent permafrost along the southern coastline.

Alaska has experienced substantial warming in recent decades. Between 1950 and 2018, mean annual air temperature increased by 2.1°C, with winter warming reaching 4.1°C [46]. Permafrost temperatures have risen by up to 0.8°C per decade since the 1980s [47–49], increasing Active Layer Thickness by more than 0.2 m in the interior and enhancing hydrological connectivity [11].

This study focuses on Alaska, because it is underlain by continuous and discontinuous permafrost and has experienced continuous expansion of industrial activities (such as oil and gas exploration since the discovery of the Prudhoe Bay oil field in 1967). Alaska and Canada contain about 23% of the total amount of contaminated sites in permafrost dominated areas [5], more than 70% of the sites are located in Russia. Alaska contains about 8620 contaminated sites of which about 3600 are located on permafrost (Fig. 1) which were listed by the ADEC [50].

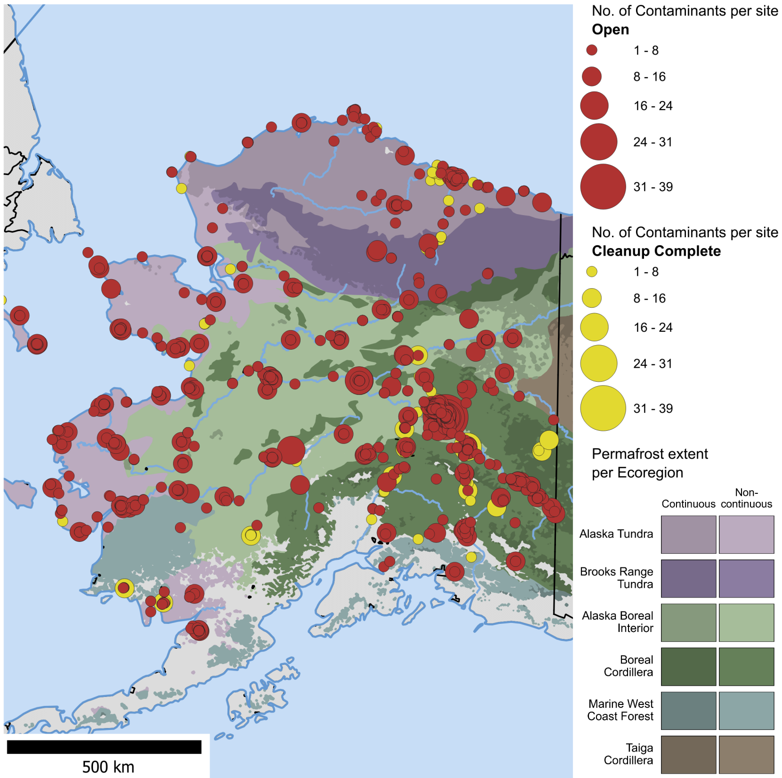


**Fig 1. Number of contaminants per contaminated site and ecoregions (Level 2) for Alaska.** The majority of the sites has ¡8 contaminants (> 84%), with a small no. of contaminated sites containing between 8 and 24 (approximately 14%). Note also the large cluster of contaminated sites around Fairbanks, with sites up to 39 contaminants. The sites that have been cleaned up but are still under institutional control have been denoted in yellow (21% of the sites). The sites that have been cleaned up and are no longer monitored are not taken into consideration for this figure.

# Materials and methods

## Datasets

### Sirius database

We use an earlier version of the SIRIUS database that covered only Alaska (nov. 2024) [51]. This database contains an expanded contaminated site database from the Alaska Department of Environmental Conservation [50], and includes identified contaminants present at the contaminated sites.

The ADEC has listed 8620 contaminated sites across Alaska, of which 42% are located in permafrost regions (occurrence probability > 0% [44]). Approximately 60% of these ($\sim$ 2100 sites) have not been cleaned up (as of 2024) (See Fig 1). Most sites are located in sporadic (52%, 1112 sites) and discontinuous (24%, 512 sites) permafrost zones, with fewer in continuous permafrost (14%, 296 sites).

The number of listed contaminants per site ranges between 1 and 39, with 70% of sites containing three or fewer contaminants (Fig 1). Sites with a higher number of contaminants are mainly located in central Alaska, particularly around Fairbanks. Contaminated sites are concentrated near industrial areas and settlements (e.g. Fairbanks, Prudhoe Bay, and Utqiagvik (Barrow)), along main transport routes such as the Dalton Highway and Trans-Alaska pipeline and near major rivers including the Yukon and the Susitna. Additional clustering occurs along the northern and western coasts.

Approximately 35% of the sites are military installations, followed by airfields (9%) and residential areas (5%). Other site types include landfills, wastewater facilities, mining operations, hospitals and oil production sites.

A total of 137 contaminants have been identified at sites located in permafrost regions (Fig 1). Hydrocarbons (diesel-range (DRO and gasoline-range organics (GRO)) are the most common contaminants, along with compounds such as benzene, toluene and xylene. Other frequent contaminants include light hydrocarbons (e.g. methane, ethane, propane) and metals, including both heavy metals (e.g. lead, zinc, cadmium, mercury) and toxic elements such as arsenic. A full list of all the contaminants listed can be found in the dataset available on Zenodo (see section Data-availability).

### Waterbodies

To gain insight into the nearest water bodies we used multiple datasets to include the different types of water bodies in Alaska. The HydroLAKES dataset provided spatial information on lakes with a surface area greater than ten hectares [52]. The Global River Widths from Landsat (GRWL) database with a spatial resolution of 30 m covered the spatial information for rivers [53]. The Global Surface Water data set by the European Commission's Joint Research Centre covered all coastal and inland surface water with a 30 m spatial resolution [54]. Finally, we used the water polygons data set from OpenStreetMap to cover oceans and seas. Through the availability of this data and the determination of the drainage pathways at each of the CS, we could infer the water body (WB) type (lake, river, and ocean) into which the contaminants would enter first in the event of mobilisation. See section Data-availability for the data repository.

## General framework to quantify the contaminant mobilisation risk

To quantify the present and future contamination mobilisation risk of permafrost-affected land areas in Alaska, we assumed that contaminants are mobilized within the thawed and water-saturated part of the ground. Here, toxic substances can be dissolved into water and distributed to the environment through lateral flow through porous soil. To assess the risk posed by the potential mobilisation of contaminants into aquatic systems we quantify a mobilisation risk for each contaminated site (CS) which is factoring in (i) the properties of the contaminants present at the site, (ii) the distance between the CS and the closest WB, and (iii) the annual groundwater discharge. Specifically, we define the hydrological contaminant mobilisation risk (R) for each CS as follows:

$$R = \tau \cdot S \cdot w_D \cdot Q \tag{1}$$

where $\tau$ and S denote the toxicity and solubility of the contaminants present at the site (CS), $w_D$ is a factor scaling the distance (D) between the CS and the closest WB (Fig. 2), and Q is the potential groundwater discharge integrated over one year. We assume that the contaminant properties and distance are stationary and site-specific, whereas the groundwater discharge is considered to change in dependence of the climate. To distinguish between stationary site-specific and climate-driven factors, we express the mobilisation risk as the product of the aquatic hazard potential ($\Omega$), and the hydrological mobilisation potential ($\Phi$):

$$R(y) = \Omega \cdot \Phi(y) \tag{2}$$

where $y$ is the calendar year, denoting the climate-dependence. The following subsections detail how we have quantified the aquatic hazard potential (Eq. 3), and the hydrological mobilisation potential (Eq. 12), respectively.

## Aquatic hazard potential of the contaminated sites

The aquatic hazard potential ($\Omega$) was derived for each CS based on information on the hazard potential of the present contaminants, and on the topographic setting of the CS and the closest WB. Specifically, $\Omega$ was calculated as

$$\Omega = \max_{i \in c}(\tau_i \cdot S_i) \cdot w_D \cdot m \tag{3}$$

Here, $\tau_i$ and $S_i$ denote normalized toxicity and solubility indices of each of the contaminants present at the site (CS), $w_D$ is a factor scaling the distance (D) between the CS and the closest WB. $m$ denotes the mean terrain slope between CS and WB which is a site-specific factor scaling the groundwater discharge Q.

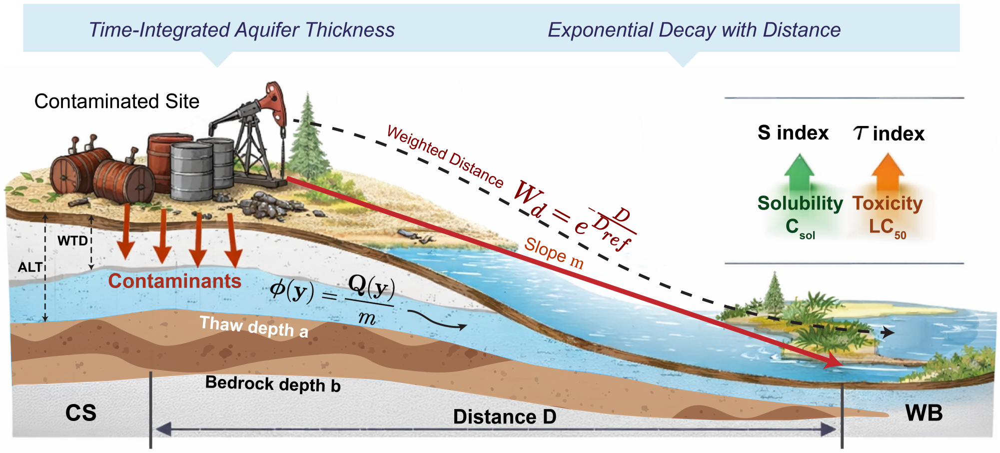


**Fig 2. Schematic overview of components of the Aquatic mobilisation potential**. Where the Aquatic mobilisation potential $\Phi$ is the modelling outcome of the CryoGridLite model. Other variables are site specific factors such as Toxicity and Solubility and Distance to WB. The slope was calculated as the elevation difference between the CS and it's closest WB.

### Toxicity and solubility of the contaminants

By using $LC_{50}$ fish, we capture the acute aquatic toxicity and provide a standardised measure that is widely applied in ecological risk assessment (e.g. [55]). Though acute toxicity does not account for chronic, sub-lethal or mixture effects, it serves as a conservative indicator of ecological sensitivity.

Toxicity data were primarily obtained from IFA – Institut für Arbeitsschutz der DGUV (2026): GESTIS-Stoffdatenbank, Deutsche Gesetzliche Unfallversicherung, available at: https://gestis-database.dguv.de (accessed 10-2025) [56] and PubChem - National Library for Medicine [57] (see the data repository available under section Data-Availability for a complete list of all references per contaminant). Each CS was assigned an aquatic toxicity index ($\tau$) based on the contaminant of concern listed in the database compiled from these sources. Toxicity was determined using the median lethal concentration in water over a 96-hour exposure period ($LC_{50}$ for fish, $96h$), according to the Globally Harmonized system [58]. The values were divided into four classes: low ($LC_{50}$ for fish between 100 and 1000 $mgL^{-1}$), medium ($LC_{50}$ for fish between 10 and 100 $mgL^{-1}$), high ($LC_{50}$ for fish between 1 and 10 $mgL^{-1}$), and very high ($LC_{50}$ for fish below 1 $mg\,L^{-1}$). In addition, substances with missing toxicity data were classified as "Unknown" (approximately 7% of the contaminants).

The toxicity index $\tau$ for a given contaminant was calculated based on lethal concentration values as:

$$\tau = \frac{\log\left(LC_{50,\max}\right) - \log\left(LC_{50}\right)}{\log\left(LC_{50,\max}\right) - \log\left(LC_{50,\min}\right)} \qquad (4)$$

where $LC_{50,\max}$ and $LC_{50,\min}$ are the maximum (lowest) toxicity contaminant and minimum (highest) toxicity contaminant respectively over all the sites. $LC_{50}$ is the $LC_{50}$ in $mg\,L^{-1}$ of the contaminant. That is, $\tau = 0$ for the least toxic contaminant (Ethylene Glycol, 54700 $mg\,L^{-1}$), and $\tau = 0.97$ for the most toxic (Benzo(a)anthracene, 0.000877 $mg\,L^{-1}$). Logarithmic scaling was applied to reduce the several orders-of-magnitude variability in aquatic toxicity values and to avoid dominance by extreme values.

The solubility index assigned to the contaminants was mostly (¿60%) extracted from the International Labour Organization - International Chemical Safety Cards database (available at: https://www.ilo.org/resource/other/ilo-who-international-chemical-safety-cards-icscs) [59], while the remainder was either extracted from IFA – Institut für Arbeitsschutz der DGUV (2026): GESTIS-Stoffdatenbank, Deutsche Gesetzliche Unfallversicherung, available at: https://gestis-database.dguv.de (accessed 10-2025) [56] and PubChem - National Library for Medicine [57] (see the data repository available under section Data-Availability for a complete list of all references per contaminant).

If an exact number for the solubility was not given, the ICSCs database denoted them with ‘very poor’, ‘poor’, ‘moderate’, ‘good’ or ‘very good’ solubility. According to their database this classification coincides with a solubility range of $< 1\ g\,L^{-1}$ (‘very poor’), $1 - 10\ g\,L^{-1}$ (‘poor’), $10 - 100\ g\,L^{-1}$ (‘moderate’) and $100 - 1000\ g\,L^{-1}$ (‘good’). Solubilities $0.001\ g\,L^{-1}$ are classified as ‘insoluble’, and ‘miscible’ for contaminants that are liquid and could mix with water. We used the ICSCs classification to assign a numerical value based on these solubility ranges as follows: $0.0001\ g\,L^{-1}$ (‘insoluble’), $0.5\ g\,L^{-1}$ (‘very poor’), $5\ g\,L^{-1}$ (‘poor’), $50\ g\,L^{-1}$ (‘moderate’) and $500\ g\,L^{-1}$ (‘good’) for contaminants that did not already have a numerical value. Miscible contaminants were given a very high number to reflect their potential mobility ($1000\ g\,L^{-1}$), while preserving the relative scaling.

Similar to the toxicity, the solubility index was scaled logarithmically and normalized to values between zero and unity as

$$S = \frac{\log\left(C_{\mathrm{sol}}\right) - \log\left(C_{\mathrm{sol,min}}\right)}{\log\left(C_{\mathrm{sol,max}}\right) - \log\left(C_{\mathrm{sol,min}}\right)} \tag{5}$$

where C is the solubility of the contaminant in $g/100mL$ and $C_{\max}$ and $C_{\min}$ are the maximum and minimum solubilities in the contaminant database respectively. That is, $S = 0.088$ for the contaminant with the lowest solubility (Aroclor 1248, $5.4 \times 10^{-06}\ g\,100mL^{-1}$), and $S = 0.966$ for fully miscible contaminants (e.g. Ethylene glycol, $1000\ g\,100mL^{-1}$).

For sites containing multiple contaminants, the aquatic hazard potential was defined by the most hazardous contaminant present, i.e. $\tau \cdot S = \max\limits_{i \in c}\left(\tau_i \cdot S_i\right)$. This conservative assumption focuses on the contaminant of greatest potential concern and ignores risks related to cumulative toxicity, mixture effects and less toxic substances regardless of their solubility and concentration.

### Topographic setting

Besides the properties of the contaminants present at the CS, the aquatic hazard potential (Eq. 3) is affected by the local topographic setting which is considering the presence of water bodies in the vicinity of the CS. We assumed that the aquatic hazard potential is decreasing with an increasing distance between the CS and the hydrologically closest WB. To reflect this decreasing hydrological connection as well as dilution effects during mobilisation along the hydrological pathway we chose an exponential decay term $w_D$.

$$w_D = \exp\left(-\frac{D}{D_{ref}}\right), \tag{6}$$

where $D_{ref} = 500m$ is a reference distance which was set as a compromise between local-scale hydrological relevance and DEM resolution. $D$ (m) is the distance along the hydrological path along the steepest gradient, which was derived in GIS, between the CS and the hydrologically closest WB. We used the ArcticDEM at a 32m spatial resolution [60] to retrieve the shortest path according to the method by Ocallaghan [61], which assigns the path of water flow from one grid cell of the DEM to exactly one of the eight neighboring cells which have the steepest down-slope gradient. To prevent depressions or pits and flat terrain with zero slopes, we preprocessed the ArcticDEM and applied the epsilon filling method from the RichDEM Python library [62]. Then the distance D between the CS and WB was set to the total length of the determined shortest path.

In addition, we extracted the difference in altitude $\Delta h$ between the CS and the WB. With this, we determined the mean slope along the hydrologically shortest pathway as

$$m = \frac{\Delta h}{D}, \tag{7}$$

Due to inaccuracies and different spatial resolutions of the input datasets (see previous section), some CS were located within their nearest water bodies. For these sites, the distance was fixed at $D = 16$m to retain a finite and realistic estimate of $\Omega$. The slope was assigned a value of 0.051, corresponding to the $98^{th}$ percentile of all calculated slopes. This value is relatively high without being extreme, ensuring a finite yet conservative estimate $\Omega$.

## Hydrological mobilisation potential

To estimate the hydrological mobilisation potential ($\Phi$), we consider an idealised setting in which permafrost-underlain terrain of a constant slope m connects the CS and the hydrologically closest WB (Fig. 2). Assuming a constant gradient in the water table, the specific discharge ($q$) per unit width of an assumed infinitely wide slope ($q$ in $m^2/s$) can be written as

$$q = \overline{K_H}\frac{\Delta w}{D}H \tag{8}$$

where $\overline{K_H}$ (m/s) is the mean saturated hydraulic conductivity within the aquifer thickness $H$ (m), $\Delta w$ (m) is the difference in water table elevation between two locations in a distance $D$ (m). In this setting, the aquifer thickness $H$ at time $t$ corresponds to the difference between the elevations of the water table ($w$ in m) and the frost table ($a$ in m; or the elevation of the bedrock $b$ (m) if the thaw depth exceeds the thickness of the soil above the bedrock):

$$H(t) = w(t) - \max\left[a(t), b(t)\right] \tag{9}$$

Assuming that the CS and the WB are sufficiently distant, the difference in water table elevation is approximated as the difference in the respective surface elevations so that $\Delta w$ can be expressed as the product of the slope ($m$) and distance ($D$) between the CS and WB. With $\Delta w \approx mD$ we can rewrite Eq.8 as:

$$q(t) = m\overline{K_H}(t)(w(t) - \max\left[a(t), b(t)\right)] \tag{10}$$

To obtain the annual lateral discharge $Q$ ($m^3/m$) per unit width across the slope, we integrate Eq. 10 over one calendar year ($y$) and obtain:

$$Q(y) = \mathrm{m}\int_y \overline{K}_H(t)(w(t) - \max\left[a(t), b(t)\right]dt \tag{11}$$

To separate the climate-dependent (time-varying) from the topographic (assumed to be stationary) factors (the slope ($m$)), we define the hydrological mobilisation potential as:

$$\Phi(y) = \frac{Q(y)}{m} \tag{12}$$

While $\Omega$ was estimated for each CS, $\Phi(y)$ was quantified for the entire permafrost region of Alaska based on model simulations.

### Model simulations and forcing data

The climate forcing used to drive the CryoGridLite model consists of three parts, (i) the spin-up period which allows the soil temperatures and other variables to adjust to prescribed initial climatic conditions, (ii) the historical period (1980-2020), and (iii) the future projections (2021-2100). The forcing for the spin-up and historical periods are based on hourly ERA5 reanalysis data with a spatial resolution of 31 km [63] . The forcing for the spin-up period was generated by repeating the meteorological data of the first decade of the historical period (1980-1989) three times. For the future projections, we applied decadal monthly anomalies from the MPI-ESM1.2-HR Coupled Model Intercomparison Project Phase 6 (CMIP6) projections [**?**] for the SSP1-2.6 and SSP5-8.5 emission scenarios to a baseline period (2011-2020) of the ERA5 reanalysis data [63, 64]. Specifically, we adjusted the MPI-ESM1.2-HR data [65], which has a spatial resolution of 0.94 ° or 100 km, using a nearest neighbour interpolation to fit the resolution of the ERA5 grid. Following Koven et al. [66], we treated the meteorological variables air temperature at 2 m, specific humidity, surface air pressure, and wind speed as additive – and the total precipitation, short-wave radiation and long-wave radiation as multiplicative anomalies. We further imposed physical constraints to exclude unphysical values such as relative humidity > 100% or negative wind speeds after applying the anomalies.

For ground stratigraphies and other parameters we followed the model setup in Langer et al. [5], where data was taken from the ECOCLIMAP global database of land surface parameters [67, 68] and additional data on soil organic carbon contents from the Northern Circumpolar Soil Carbon Database version 2 [69] as a basis for generating ground stratigraphies. The thickness of the soil layer above the bedrock was derived from the Gridded Global Data Set of Soil Thickness [70]. We based our default values for the parameters related to the surface energy balance (albedo, emissivity, roughness length), as well as the parametrisation of snow albedo change, on those of Westermann et al. [71]. The values for hydraulic conductivity required to calculate $\overline{K}_H$ were obtained using parametrizations based on pedotransfer functions by Clapp & Hornberger [72] developed for the SURFEX land surface model [73].

We used the CryoGridLite permafrost model [74, 75] to simulate the ground thermal and hydrological regimes across Alaska under different climate scenarios. CryoGridLite solves the one-dimensional heat diffusion equation taking into account the phase change of soil water, as well as the dynamic build-up and ablation of a seasonal snow pack. Similar to Chen et al. [76], we used a version of CryoGridLite that was extended by a surface energy balance calculation and a simple subsurface hydrology scheme.

We conducted two sets of simulations (Table 1). First, we ran a parameter-ensemble of simulations with an ensemble size of $N = 200$ in which eight model parameters for six selected sites were randomly varied. These simulations were run for the spin-up and historical periods and then used to assess the model sensitivity and evaluate the model performance by comparing to observational data available for these sites (see Supp. Material S3). The model evaluation revealed an overall satisfying capability of the parameter ensemble to capture the active layer dynamics at the six selected sites (Fig. S3.1), and the water table depth at the site Utqiagvik (Barrow) in northern Alaska (Fig. S3.2). For the same site, the model sensitivity was systematically explored. For this, we considered the difference between the ALT and WT (at the time of maximum ALT) which corresponds to the thickness of the fully saturated part of the active layer. We found by far the strongest correlation ($R^2 = 0.88$) with the volumetric organic content in the upper 0.3 m of the ground (VSOC; see Fig. S3.3). Note that VSOC is directly related to VMC in Table 1, as the two parameters were co-adjusted so that the soil porosity in the upper 0.3 m ($\varphi$) was held constant according to the input data (i.e. VSOC = 1 - VMC - $\varphi$). A doubling of VSOC resulted in an about 30% reduction of WT-ALT. For the remaining parameters the correlations were not significant.

Based on the insights from the model evaluation and sensitivity analysis, we then ran a second set of simulations with a single parameter setting for each of the gridcells covering the permafrost-affected regions of Alaska which included the spin-up, historical, and future projections periods. For these simulations we chose default values for most of the varied parameters around the mean value of the ensemble range (Table 1), while we set the maximum snow height to the maximum of the ensemble range and the residual water factor to the minimum of the ensemble range, since this value corresponds more closely to the literature values for residual water content [77, 78]. Since the model evaluation based on ALTs did not suggest a clear preference for simulations with higher or lower VSOC (Fig. **??**), we decided to set VSOC halfway between the minimum and maximum values of the ranges explored in the ensemble simulations. For this choice of default parameter values, the spatial simulations of contemporary ALTs in Alaska resemble the permafrost zonation according to the map by Obu et al. [44] fairly well (See Fig. 4).

From the second set of simulations, we diagnosed the hydrological mobilisation potential ($\Phi(y)$) across the simulation domain in Alaska for each calendar year. For this we calculated the aquifer height ($H(t)$) using Eq. 9 and used the daily frost table ($a(t)$) and the water table ($w(t)$) as simulated by the model. $\overline{K}$ in Eq.10 was calculated as follows

$$\overline{K} = \frac{\sum_{i=0}^{n} \Delta\, d_\mathrm{i}\, K_\mathrm{i}}{\sum_{i=0}^{n} \Delta\, d_\mathrm{i}} \tag{13}$$

where $n$ is the number of soil layers, $\Delta\, d$ (m) is the thickness of a subsurface soil grid layer and $K$ ($\mathrm{m\,s^{-1}}$) is the hydraulic conductivity of this soil layer. The values for hydraulic conductivity required to calculate $\overline{K}$ were obtained using parametrisations based on pedotransfer functions by Clapp & Hornberger [72] developed for the SURFEX land surface model [73].

**Table 1.** Parameter values used in the CryoGridLite simulations for model evaluation, sensitivity analysis, and $\Phi$ projections.

| Parameter | Model evaluation and sensitivity | | $\Phi$ projections |
|---|---|---|---|
| | Min. | Max. | Default |
| Volumetric mineral content (upper 0.3 m; VMC) | 0.05 | $\theta_{\mathrm{m}}^{\mathrm{ECOCLIMAP}}$ | $\left(0.05 + \theta_{\mathrm{m}}^{\mathrm{ECOCLIMAP}}\right)/2$ |
| Field capacity factor ($f_{\mathrm{fc}}$) | 0.25 | 0.75 | 0.5 |
| Residual water factor ($f_{\mathrm{w}}$) | 0.10 | 0.15 | 0.10 |
| Evaporation depth ($d_{\mathrm{e}}$) [m] | 0.05 | 0.20 | 0.10 |
| Maximum snow height [m] | 0.2 | 2.0 | 2.0 |
| Soil albedo ($\alpha_{\mathrm{s}}$) | 0.1150 | 0.3544 | 0.20 |
| Roughness length soil ($z_{0,\mathrm{soil}}$) [m] | 0.0005 | 0.0015 | 0.001 |
| Emissivity soil ($\epsilon_{\mathrm{soil}}$) | 0.9428 | 0.9987 | 0.97 |

## Use of artificial intelligence tools

We used AI tools (GPT-5.2, OpenAI) in a limited and supporting role during this study. It was used to generate the background of Fig. 2, however, all the scientific annotations, arrows, labels and overlays were created manually by the authors. AI tools also provided support in Python coding for figure and map creation and it was used to assist in spelling, grammar and language refinement of the manuscript. All AI-generated outputs were critically evaluated, manually reviewed and revised by the authors. Scientific interpretations, results, conclusions, and manuscript content represent the authors' own work and were not generated by AI.

# Results

## Components of the Aquatic Hazard Potential

Approximately 40% of the contaminants exhibit a poor solubility (see  for classification), while 25% are considered insoluble. This includes PCBs, Metals and Pesticides and Herbicides. About 5 contaminants are considered as 'miscible' (e.g. some Organic compounds and Cyanide) and only a few contaminants have a moderate solubility at 20°C (PFAS) ($\sim$ 5%). 3 metals react with water (e.g. Barium), instead of dissolving.

Pesticides and Herbicides are highly toxic (ranging from 'high toxicity': $1 - 10\ mg\,L^{-1}$, to 'very high toxicity': $< 1\ mg\,L^{-1}$, according to the Code of Federal Regulations [58]. Other highly toxic contaminants include Cyanide, metals and a group of PAHs.

In addition, while there are relatively few CS with pesticides and herbicides (44 sites with very highly toxic components), their impact on the environment is large. Most of these contaminants are highly persistent with long-lasting effects on the environment and have very high toxicities (See the data repository available under section Data-Availability for a complete list of toxicity per contaminant). 34 sites contain highly toxic metals, while another 31 sites contain very toxic PAHs.

Fig. 3 shows that there are no clear patterns between the variables, except for the hydrological mobilisation potential, which shows some clustering between different ecoregions. This is caused by the fact that $\Phi$ is dependent on climatic factors, which vary between ecoregions (but not so much inside ecoregions).

The mobilisation of contaminants is denoted by the distance that a contaminant has to travel to contaminate a larger WB. The nearest WBs were classified as lakes, rivers, or the ocean. Smaller scale streams were not included due to the resolution of the river database (30). The majority of sites (70%) were closest to a lake, followed by rivers (22%) and the ocean (8%). Most sites are located within 1 km of the nearest WB (40% of lake sites, 35% of river sites, and 70% of ocean sites). Of sites which are located closest to the ocean, 64% lie within 500. In comparison, only 30% of lake and river sites are located less than 500

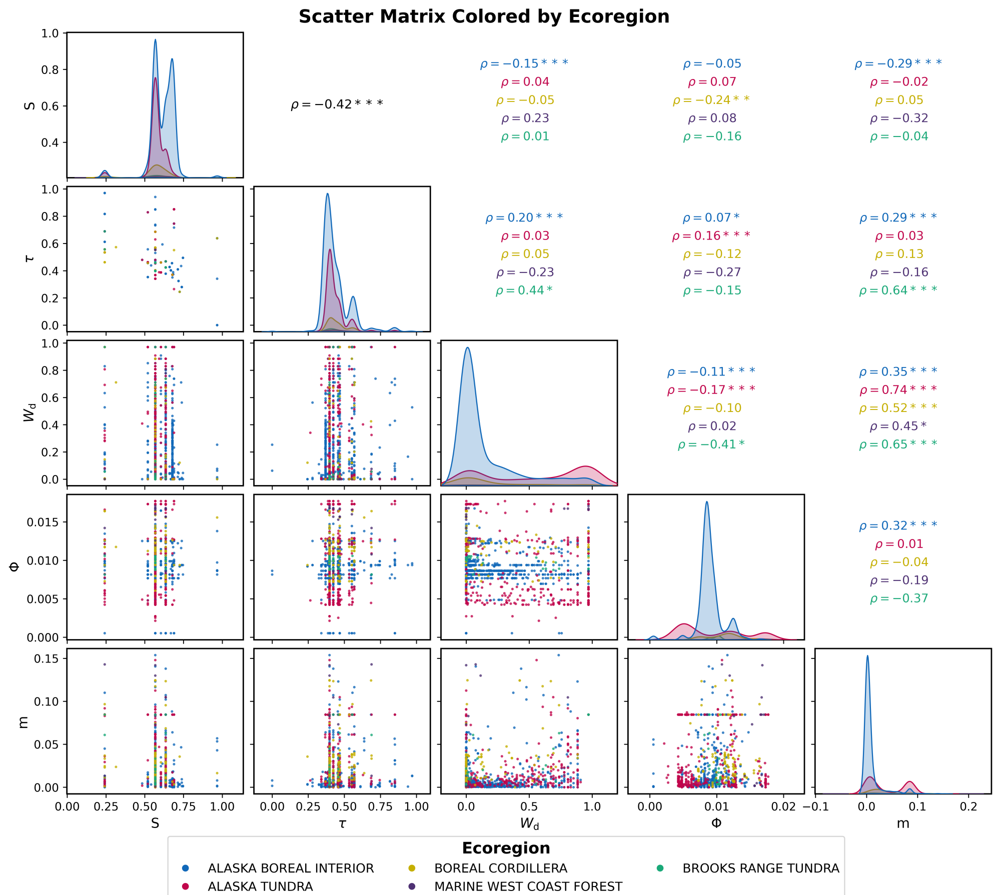


**Fig 3. Scatter Matrix plot of Aquatic mobilisation risk variables with Spearman correlation per ecoregion**. Where each variable is plotted against the other variables to show possible correlations. The mobilisation potential $\Phi$ shows some differences between ecoregions since it is dependent on climatic factors, which vary per ecoregion. There are no clear correlations between variables except for the slope $m$ and the weighted distance $w_D$ which are dependent on each other (see Eq. 7)

away from their closest WBs. These results indicate that the potential for contaminant mobilisation via hydrological pathways is high, particularly for sites adjacent to the ocean. By taking the weighted distance (Fig. 3) sites located further away than the reference distance of 500, get progressively lower $w_D$ values (Fig. 2). This means that most ecoregions show low $w_D$, with the exception of the Alaska Tundra, where the majority of the sites are located closer to their WBs.

For sites located within WBs, the distance was set to 15. In total, nearly 250 sites (12% of all sites) were identified as submerged, indicating that contaminant mobilisation may already be occurring independent of additional hydrological changes.

## Simulated hydrological regime and mobilisation potential ($\Phi$)

The distribution of the hydrothermal mobilisation potential ($\Phi$) is strongly controlled by both the active layer thickness and the watertable (see Fig. 2). These variables were simulated using the CryoGridLite model (see ) for present-day conditions as well as future climate predictions (SSP1-2.6 and SSP5-8.5).

Future climate predictions show a continued increase in air temperature across all five ecoregions, with mean warming rates of approximately 0.2°C/decade under SSP1-2.6 and 0.7°C per decade under SSP5-8.5. The Alaska Tundra ecoregion shows the strongest warming (0.22 and 0.81°C per decade under SSP1-2.6 and SSP5-8.5 respectively), whereas the Marine West Coast Forest shows the lowest overall warming rates (0.19

and 0.59°C per decade).

Precipitation trends differ between scenarios. During the first half of the century, total precipitation is generally lower under SSP5-8.5 than SSP1-2.6, particularly in the Boreal Cordillera and the Marine West Coast Forest. The largest increases in total precipitation occur in the Marine West Coast Forest under both scenarios, whereas the Alaska Tundra shows comparatively small increases. Across all ecoregions, precipitation type shifts toward more rainfall and less snowfall, largely driven by rising temperatures. The Brooks Range Tundra, Marine West Coast Forest and the Alaska Boreal Interior experience the largest rainfall increases. Snowfall declines are strongest in the Marine West Coast Forest and Alaska Tundra, while the Brooks Range Tundra shows only minor snowfall decreases under SSP5-8.5 and even slight increases under SSP1-2.6.

ALT shows a pronounced north-south gradient (Fig. 4), with shallow active layers in northern Alaska and deeper thaw in the south. This pattern largely reflects the mean annual air temperature and is locally modified by topography, with mountain ranges such as the Alaska Range showing reduced ALT due to elevation effects. Future projections indicate widespread ALT deepening across Alaska, with the largest increases occurring in a west-east oriented band south of the Brooks Range. Differences between SSP1-2.6 and SSP5-8.5 remain small in the first half of the century, but diverge substantially during the second half, with SSP5-8.5 showing greater ALT deepening in mainly Northern regions.

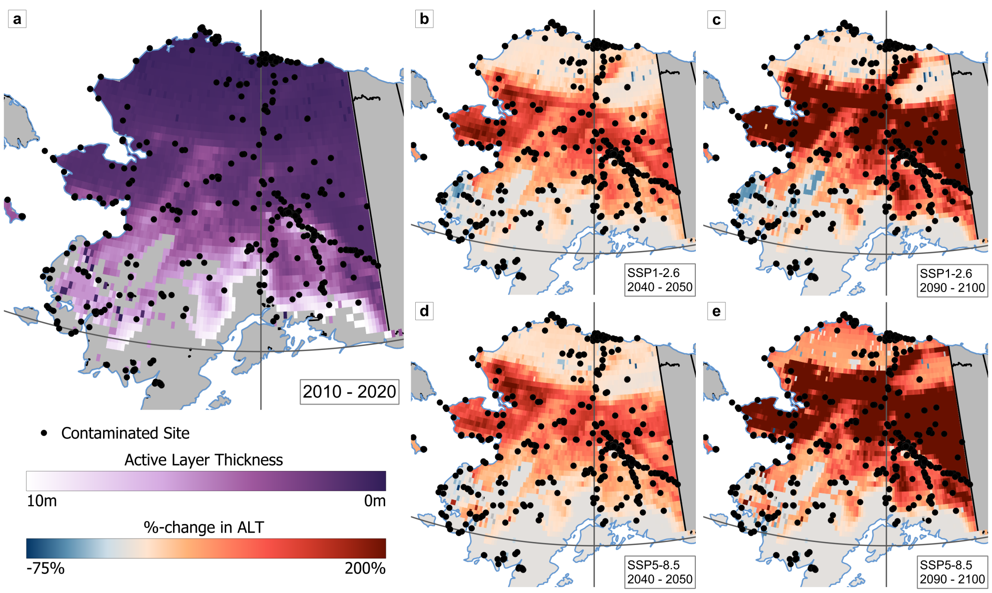


**Fig 4. Modelled ALT (CryoGridLite) for current conditions and SSP1-2.6 and SSP5-8.5 scenarios.** a) There is a strong North-South gradient in ALT caused by the MAAT. b) The northern coastline shows a more stable ALT with only minor increases under SSP1-2.6 for the first half of the century and c) for the second half of the century. d) The patterns for the first half of the century under SSP5-8.5 are similar to the SSP5-8.5 scenario. e) For the latter half of the century under SSP5-8.5 the increases in ALT are up to 100%. Under both warming scenarios the largest increases happen in the Brooks Range, with changes up to 200% under both climate scenarios at the end of the century.

ALT increases along the northern coastline and the southern margins of the permafrost zone are initially smaller, but under SSP5-8.5 these regions also experience increases exceeding 100% by the end of the century. In southern regions this may locally result in complete loss of permafrost, removing hydrological barriers and creating new flow pathways, whereas along the northern coastline it primarily results in deeper seasonal thaw. No systematic differences are observed between the western coastal regions and the interior.

Water table depth follows a broadly similar spatial pattern (Fig. 5), with deeper water tables in southern Alaska and shallower conditions in the north. A zone of relatively shallow water tables is also simulated south of the Brooks Range, a feature less pronounced in the ALT distribution. Projected changes in water table depth are concentrated mainly in this central Alaskan band. Under SSP5-8.5, water tables decline (e.g. drying) by more than 0.75 in parts of central Alaska during the latter half of the century, particularly on the Seward Peninsula and in the Yukon Tanana Uplands. In contrast, the northern coastline shows only minor drying under both scenarios, with maximum decreases of roughly 0.20 by the end of this century under the SSP5-8.5.

**Fig 5. Modelled water table depth of Alaska.** Figure a) shows the current modelled conditions, while b-e) show the future predictions under different climate scenarios for both 2040-2050 and 2090-2100. The water table depth is largest in the south and smallest in the Brooks Range. Under future climate conditions Alaska shows an overall drying pattern, with the most severe drying (lowering of the water table) in central Alaska. Interestingly, similar to the ALT the water table remains fairly stable in the Alaska Tundra region in the North (along the coastline), with only increased drying for the latter half of the century under the SSP5-8.5 scenario. The SSP1-2.6 shows that there is some rewetting taking place at the second half of the century, which is most pronounced in Central Alaska.

Some of the early drying simulated under SSP1-2.6 reverses during the latter half of the century, resulting in partial rewetting. A weaker version of this trend is also present under SSP5-8.5, reflected in smaller water table declines later in the century. Along the southern margins, water table depth generally increases under all scenarios and time periods, with spatial patterns remaining largely consistent despite differences in warming trajectories.

Because $\Phi$ depends on both ALT and water table depth, its spatial distribution reflects the interaction between these variables (Fig. 6). Present-day $\Phi$ values are generally lowest in northern Alaska and highest toward the southern coastline (see Fig. 6). Under future climate projections, $\Phi$ increases across most of Alaska under both SSP1-2.6 and SSP5-8.5. The largest relative increases ($> 100\%$) occur along the northern coastline and in the Ogilvie Mountains, while southern regions also show strong increases, particularly toward the end of the century.

Under SSP5-8.5, $\Phi$ decreases during the first half of the century along the Brooks Range and parts of the western coastline. These decreases coincide with periods of increasing precipitation and reflect a lowering of the water table that offsets ALT deepening. In central Alaska, changes in $\Phi$ remain relatively modest, suggesting that increases in ALT are partly balanced by declining water tables.

## Mobilisation risk under climate change

The Aquatic Hazard potential ($\Omega$) is a site-specific metric derived from contaminant properties and site morphology and does not vary with climatic forcing. Across Alaska 87.5% of all the contaminated sites fall within the low hazard class ($\Omega < 0.018$), while 12.3% and 0.2% fall within the medium ($\Omega$ 0.018 - 0.036) and high ($\Omega$ 0.036 - 0.054) classes respectively. Although high-$\Omega$ sites are rare, some occur in regions that already exhibit high present-day $\Phi$, particularly along the southwestern coastline. Others are located in regions projected to experience strong future increases in $\Phi$, including the northern coastal regions (see Fig. 6).

When the aquatic $\Omega$ and the $\Phi$ are combined, a risk factor for each CS can be determined.

Low risk was defined as $< 4 \times 10^{-7}$, $4 \times 10^{-7}$–$1 \times 10^{-5}$(medium risk), $1 \times 10^{-5}$–$9 \times 10^{-5}$ (high risk) and $> 9 \times 10^{-5}$ (very high risk). (see Fig. 7 for site distribution per risk category and see Fig. S2 for a probability density function (PDF) plot and a cumulative density function (CDF) plot of the risk of contaminated sites).

Both scenarios show that the largest number of sites with medium and high risk for mobilisation of contaminants are located in the Alaska Tundra, the Brooks Range Tundra and the Marine West Coast Forest ecoregions. These regions encompass the northern and most of the western and southern coastline and the Brooks Range (See Fig. 7). The Alaska Boreal Interior contains the largest amount of contaminated sites, but only 10% of the sites are classified as 'high' to 'very high' risk. The Marine West Coast Forest has around 45% 'high' to 'very high' risk sites, but contains much less contaminated sites. The Brooks Range Tundra and the Boreal Cordillera have a little over 30% of 'high' to 'very high' risk contaminated sites.

For both the SSP1-2.6 and the SSP5-8.5 scenarios the amount of 'medium', 'high' and 'very high' risk sites are relatively stable for most of the ecoregions. The Alaska Tundra is the general exception, with

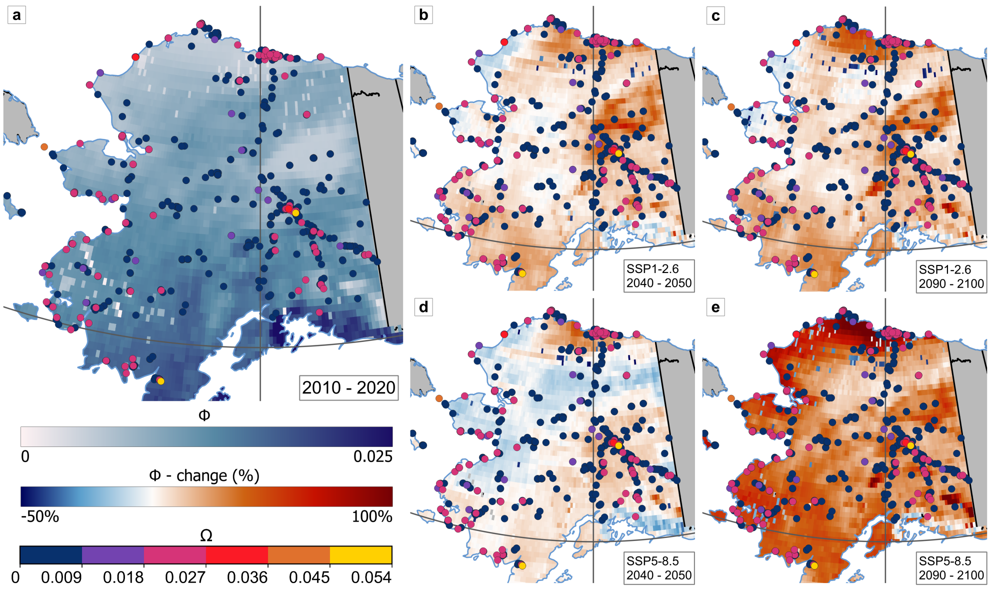


**Fig 6. Modelled mobilisation potential Φ with aquatic hazard potentials Ω of each CS.** Figure a) shows the spatial distribution of Φ (the hydrological mobilisation potential in the thawed ground) and is largely dependent on the active layer thickness, with larger values in the south. Figures b - e) show the percentage change from the 2020 baseperiod. The dots represent the Aquatic Hazard Potential (Ω) of the contaminated sites on discontinuous and continuous permafrost. Most of the potentials are fairly low, apart from sites concentrated around Fairbanks, along the Northern Coast (Deadhorse and Prudhoe bay) and along the western coastline

increases for both scenarios ($> 5\%$ compared to the baseline of 2010-2020). About half of the contaminated sites are considered 'very high' risk of contamination mobilisation (49%), which increases to up to 55% of sites at the latter half of the century under SSP5-8.5. The Alaska Boreal Interior and the Boreal Cordillera see minor increases in 'high' to 'very high' risk sites. Despite the large increases in Φ for most of Alaska under the SSP5-8.5 scenario (latter half of the century) this is not reflected in the mobilisation risk. Only the Alaska Tundra (which shows the most significant Φ increase) shows the large increases in mobilisation risk.

Approximately 50% of the sites in the Alaska Tundra are located around the Prudhoe Bay oil fields (North Slope) and 70% of the sites in the Boreal Cordillera are located around Fairbanks. Together, these two hotspots account for 57% of all contaminated sites, indicating a strong spatial concentration of mobilisation risk.

For the Prudhoe Bay oil fields there are 343 counts of medium toxicity contaminants (of a total of 634) and 60 with a high toxicity (over 10% of the Prudhoe Bay contaminants have a high to very high toxicity). Most sites have 5 or less contaminants, 4 sites have 6, 12 with 9, and 3 sites with more than 10 contaminants listed.

Around Fairbanks there are 3617 listed contaminants, with more than 460 counts of 'high' toxicity and 80 counts of 'very high' toxicity. These sites also contain more contaminants per site, with up to 39 contaminants per site (20% of the Fairbanks sites contain 6 or more contaminants).

# Discussion

## Main drivers of Aquatic Hazard potential

The Ω represents a site- and contaminant-specific estimate of the potential for aquatic contamination impact. By combining scaled toxicity ($LC_{50}$ fish, $96h$), water solubility and distance to the nearest WB, Ω encompasses three components of chemical hazard: potency, mobility and hydrological connectivity. In line

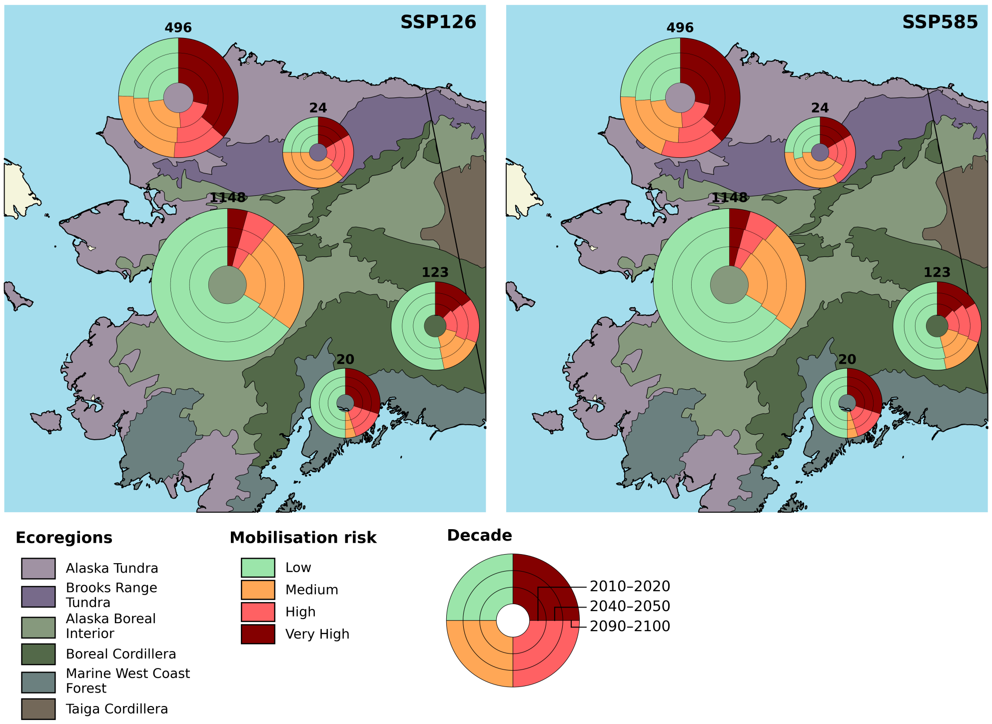


**Fig 7. Mobilisation risk per ecoregion for both the SSP1-2.6 (left) and the SSP5-8.5 (right) scenario.** Each pie chart shows the relative number of contaminated sites in each risk category per time period. The size of the pie chart indicates the total no. of contaminated sites in the ecoregion. Note that there are relatively small changes in most ecoregions, with the exception of the Alaska Tundra.

with established environmental risk frameworks, hazard reflects the capacity of a contaminant to cause adverse effects, independent of temporal exposure dynamics (e.g. [55, 79]).

Solubility is used as a first-order proxy for contaminant mobility. The dissolved fraction of contaminants indicates its availability for advective transport via groundwater flow, Active Layer drainage and overland flow processes. Compounds with higher solubilities are more readily partitioned into water and therefore more likely to be mobilised. Though solubility alone cannot capture additional processes such as sorption to organic matter, colloidal transport, non-aqueous phase liquid behaviour or degradation kinetics (e.g. [27, 55, 79–81]). $\Omega$, therefore, represents a simplified but scalable estimate of mobilisation potential.

The distance to the nearest WB acts as a function for hydrological connectivity and the hazard of wider exposure. Shorter distances reduce travel time and attenuation opportunities [79], increasing the probability of contamination of wider areas. In Arctic environments characterised by dense lake networks and shallow active layers, surface and near-surface hydrological connectivity could enhance this effect. Additionally, site-specific factors like hydrological conductivity, which are often not known on a wider scale, could be considered in detailed studies of contaminated sites to better understand groundwater flow potential under varying soil conditions. Since soil conditions are largely controlled by surface geology, they can strongly influence contaminant mobilisation. Groundwater flow potential is generally higher in coarse-grained materials such as sand and more limited in low-permeability materials like clay or unfractured bedrock, where mobilisation is more likely to occur via overland flow. However, due to the lack of site-specific geological and soil data, these factors were not included in this study, but could be considered for in depth, site-specific research.

Analysis of individual contaminants demonstrates that elevated $\Omega$ can arise from different combinations of chemical properties and spatial configuration. High $\Omega$ values coincide with both high toxicities, such as Pesticides and Herbicides (the top three sites all contain DDT), and very small distances to WBs (all three are set at 16 distance; see ), despite poor solubility. Conversely, Benzo(a)anthracene - the most toxic contaminant - shows lower Ω due to the large distances from the closest WBs (319 m - 7,6 km) and low solubility. Cyanide exhibits the highest intrinsic contamination hazard due to the very high toxicity and miscibility.

These results indicate that, while toxicity and solubility contribute to hazard, proximity to WBs is often the dominant driver of Ω.

Ω represents an estimate of potential aquatic impact, its spatial expression across Alaska depends strongly on landscape configuration and contaminant distribution.

In the Arctic Tundra ecoregion, contaminated sites are often located closer to WBs due to the high lake density [43, 82] and coastal proximity. Although hydrocarbons dominate these sites - particularly around the Prudhoe Bay oil fields - and generally have lower acute aquatic toxicity compared to other contaminant classes, their short transport distances contribute to higher Ω-values. On the other hand, sites in the Alaska Boreal Interior, and specifically the Fairbanks region, are frequently located further away from major WBs. However, the prevalence of PFAS, which has higher aquatic toxicity and solubility, increases the Ω despite larger distances.

As an example, a report from 2018, has summarized that PFAS contamination is widespread in Alaska [83]. Many consumer products contain PFAS but the major sources of PFAS releases into the environment are airports, oil and gas facilities, rail yards, military installations, industrial sites, landfills and wastewater treatment plants [83]. Here, the role of permafrost was only touched upon, stating that the presence of permafrost is crucial for groundwater hydrology. The (im-)permeability of the ground could explain the heterogeneity in measured PFAS concentrations at neighbouring drinking water wells. This suggests that high sampling rates are needed to understand local contamination.

In addition, accidental releases of PFAS into the environment led to the closure of 2 lakes for fishing, in Alaska [38]. Here the State Department of Fish and Game measured contaminant levels well above the advisory safety limits set by the Environmental Protection Agency. This led to the closure to fish as well as a suspension of hatchery fish stocking. This was the first reported closure of lakes due to PFAS contamination.

PFAS is also a contaminant that has long lasting environmental persistence, contributing to potential increased contaminant exposure [84, 85], though the longevity of contaminants is beyond the scope of this research and not included in the Ω.

This spatial contrast highlights that the Ω can be driven either by hydrological connectivity or chemical properties. In tundra regions, hydrological proximity appears to dominate, while in boreal regions contaminant toxicity and mobility play a large role. These findings highlight the importance of integrating chemical and spatial variables when assessing potential aquatic impacts.

## Hydrological and climatic controls on mobilisation

While Ω describes the intrinsic static hazard potential, contaminant mobilisation depends strongly on permafrost-controlled hydrology. Changes in Active Layer Thickness (ALT) and water table depth (WTD) are a critical factor in projected changes in hydrological mobilisation potential.

Both the ALT and the WTD show a general North-South gradient, with shallower ALT and very shallow WTD in northern regions and deeper conditions in the south. Future projections indicate increases in ALT depth and drying across central Alaska, particularly south of the Brooks Range (See Fig. 4 and 5).

Similar to this study, Yi et al. [86] found that there has been widespread ALT deepening since 2001 in Alaska. This is mainly driven by increases in air temperature and the increases in ALT were more pronounced in the discontinuous and sporadic permafrost zones. In their study, the ALT was fairly stable in the colder northern regions of Alaska, which was also found in this study.

A settlement index created by Karjalainen et al. [31] uses both a combination of climate forcing scenarios (RCP) and a local hazard potential such as ground ice content and soil properties to model the risk of infrastructure damage. Their risk and hazard assessment shows that the largest hazards occur across a central band in Alaska, just south of the Brooks Range. This is consistent with the largest changes in ALT and WTD for this research. However, this region does not have the highest risk values for contaminant mobilisation, due to the lower hydrothermal mobilisation potential (Φ) in the central and interior of Alaska.

This study shows that, while the northern coastline does experience some of the largest temperature increases (e.g. [87]), this does not coincide with the strongest increase in ALT. It suggests that air temperature alone cannot explain the large increases south of the Brooks Range. Hydro-thermal feedbacks also play an important role.

Deepening water tables can promote deeper thaw by reducing the latent heat buffering capacity of the overlying water column [88]. It is important to note, however, that the deepening of the water table depth could also be caused by the deepening of the active layer. The Active Layer acts as a barrier on which the water table is situated, with deeper Active Layers the water table will be lowered as well.

While all ecoregions show increases in annual air temperature (especially under SSP5-8.5), the Alaska Tundra and the Brooks Range Tundra show the largest increases, in addition to also experiencing increased rainfall (under both scenarios, but larger increases under SSP5-8.5). The increase in precipitation under both the SSP1-2.6 and the SSP5-8.5 are consistent with trends between 1957 and 2021 as noted by Ballinger et al. [87]. For the first half of the century SSP1-2.6 shows larger increases than the SSP5-8.5, but where this stabilises for SSP1-2.6, SSP5-8.5 continues to increase toward the latter half of the century. This means that the deepening of the water table cannot be attributed solely to the change in precipitation. Instead, rising evapotranspiration driven by increasing temperatures probably results in a net soil moisture deficit. Thunberg et al. [89] show that even though the P-ET balance is lower in the Boreal Interior of Alaska, it does still show an overall positive effect. Other studies indicate enhanced evapotranspiration across Alaska that could lead to soil drying despite increased rainfall [90, 91].

These findings suggest that increased evapotranspiration, rather than precipitation alone governs future mobilisation potential. This is also reflected in the hydrothermal mobilisation potential ($\Phi$), that shows different spatiotemporal patterns than both the ALT and the WTD.

A Pan-Arctic study on the hazards of infrastructure damages [30, 92] show that the southern permafrost regions in Alaska are a hotspot. They attribute this to relatively high ground ice-contents, frost-susceptible sediments and an increased potential for permafrost thaw. This is consistent with the large hydrothermal mobilisation potential found in the South of Alaska (Fig. 4).

Under the SSP5-8.5 scenarios $\Phi$ decreases for the first half of the century, while it increases for the SSP1-2.6. This pattern is also visible in Hjort et al [30], where thaw-induced ground instability is similar for the first half of the century regardless of the GHG emission scenario. The differences in $\Phi$ during the early period cannot be explained solely by thaw dynamics. Instead, precipitation differences appear to play a role. Between 2020 and 2060, mean annual precipitation in the study region is projected to be roughly 8% lower under SSP585 than SSP126, only exceeding SSP1-2.6 values after 2060. Tebaldi et al. [93] similarly found slightly higher precipitation in SSP1-2.6 during the early century across CMIP6 projections.

Because this study uses a single climate model (MPI-ESM 1.2-HR [65]) and focuses on the Alaskan permafrost domain, uncertainty remains regarding the robustness of these differences. Nonetheless, multiple studies indicate overall precipitation increases across Alaska [87, 89–91].

## Spatial-temporal variations in Mobilisation Risk

Where the hydrothermal mobilisation potential ($\Phi$) shows a gradual north-south pattern, with larger potentials in the South and lower potentials in the North, the largest increases happen mostly along the northern coastline. This is also visible in the mobilisation risk where the Arctic Tundra and Brooks Range Tundra have the largest contribution of 'very high' and 'high' risk contaminated sites. This is consistent with findings of Anisimov and Reneva [94] who also show the largest hazards along the Northern coastline of Russia for infrastructure damages due to permafrost thaw (particularly due to changes in ALT). Nelson et al. [95] also show that the largest increases in risk of infrastructure damage due to permafrost thaw, is along the northern coastline for Alaska and to a lesser extent for Northern Russia.

The large increases in number of sites with 'high' to 'very high' mobilisation risk for mid- and late century climate scenarios also confirms the estimate by Langer et al [5] that a growing number of industrial infrastructure sites and contaminated sites in the Arctic could be affected by permafrost degradation. While the hotspots with high risk contaminated sites are located mostly in the Arctic Tundra and the Brooks Range Tundra ecoregions. The sites with the largest mobilisation risk are located in the south (2 sites) and in Fairbanks (1 site). To illustrate how the combined chemical and climatic drivers operate at individual locations, a few high-risk sites were examined in detail.

### King Salmon Contaminated sites with very high risk

Sites 706 and 707 in King Salmon (Bristol Bay) exhibit the highest mobilisation risks under both SSP scenarios, with mobilisation risks of 0.0010 and 0.0011 under SSP1-2.6 and SSP5-8.5 respectively.

Site 706 is a military installation (base/post/other) and 707 is an accompanying landfill (Tab. S1; ADEC_ID_706 & ADEC_ID_707_2009). They are located on the river banks of the Naknek river, which drains from the Naknek Lake into Kvichak Bay. King Salmon is located in the south-west of Alaska in the Bristol Bay - Nushagak Lowlands and classified as Alaska Tundra [45]. Despite this the permafrost layer consists of isolated patches [96].

These sites were specifically meant as an off-base recreational facility of the King Salmon Air Station and were established in 1952 and used until 1977. Facilities included equipment for outdoor use (boat docks, fish camps, lodging etc) as well as a landfill and a fuel storage area (Tab. S1; ADEC_ID_706 & ADEC_ID_707_2009).

Hazardous substances around the area are contaminants like diesel fuel, gasoline, oil, antifreeze, solvents, pesticides and polychlorinated biphenyls. In 1998 remedial actions were taken to prevent contamination of the area. This includes excavation of contaminated soils (up to 1.5 m depth) and capping with clean soil and vegetation as well as disposal of solid waste, removal of septic tanks, capping of the landfill area, installation of groundwater monitoring wells and the collection of water samples and surface soil samples (Tab. S1; ADEC_ID_706 & ADEC_ID_707_2009).

Current environmental concerns (after clean-up) consist of remaining Diesel-Range-Organics (DRO) contaminated soils and exposure of contaminants if the landfill cap vegetation is disturbed. Groundwater monitoring revealed no contamination since 1994. Since 1999 the site has been under institutional control, with land use restrictions (mainly for drinking water wells and soil excavation). The landfill cover is maintained and inspected regularly and groundwater is continuously monitored (Tab. S1; ADEC_ID_706 & ADEC_ID_707_2009).

The high aquatic contaminant mobilisation risk is caused by the extremely toxic contaminants present here, such as DDT (but it also includes other contaminants such as DRO and Gasoline-Range-Organics (GRO)) for both sites (Tab. S1; ADEC_ID_706, ADEC_ID_707_2009, ADEC_ID_707_2021). Due to their close proximity to the river, transport over wider areas is easily achieved during mobilisation. The groundwater flow potential is among the highest modelled and is expected to increase with more than 25% at least (up to 100% for the latter half of the century under the SSP585 scenario), this combined with the high aquatic hazard potential ($\Omega$) results in a very high mobilisation risk.

However since this site has been cleaned up after 1999 the risk has been reduced. The most important contaminant still found there is DRO which has been found below the previously excavated contaminated soil (Tab. S1: ADEC_ID_707_2021).

### Eielson Contaminated Site with very high Aquatic Hazard Potential

High mobilisation risk is partly driven by the Aquatic Hazard Potential, and site 392 has the largest $\Omega$ of all contaminated sites addressed in this study. This contaminated site is also a military installation and classified as an air force base in the city of Eielson. Site 392 is specifically used for Asphalt mixing and is still considered an active site (Tab. S1; ADEC_ID_392_1995, ADEC_ID_392_2018). Eielson is located in the region around Fairbanks in the Alaska Boreal Interior [45] on sporadic [96] permafrost. It is located in the floodplain of the Tanana River.

From the 1950 until the 1960 the site was used as an asphalt cement mixing area and about 200 empty drums were disposed of in this area. Waste oils and solvents were mixed with contaminated fuels for use in road oiling against dust. The area also has been used for mixing pesticides, as is apparent by the presence of pesticides such as DDT, DDD and DDE. The site report also indicates that Aldrin, Alpha-BHC, Chlordane and Heptachlor Epoxide have been found on site (Tab. S1; ADEC_ID_392_1995). Soil samples revealed up to 62.5 and 58.6 mg/kg of DDT and DDD respectively. These concentrations are just below the $LD_{50}$ rat (87 mg/kg and 113 mg/kg, respectively). The concentrations of DDD and DDE in groundwater were below the detection limits (Tab. S1; ADEC_ID_392_1998).

As remedial measures for (further) contamination it was proposed to cover the soil and to remove the drums. A clean cover would prevent contact with the pesticides and prevent runoff in the Garrison Slough pond. Drums that were buried were left in place and groundwater, surface water, the soil and aquatic organisms were monitored. Therefore, since 1997 over 1100 drums were removed and detected PCBs in 2016 were excavated as well. Groundwater monitoring indicated that there were no VOCs or pesticides detected after 2016 (Tab. S1; ADEC_ID_392_1998, ADEC_ID_392_2018).

Evaluation of the site suggested that there was an acceptable risk to human health or the environment. The highest concentrations of pesticides were only found in isolated instances and not consistent over the area. Since the potential for residential development in this area was very low, the risk of human exposure was also fairly low. More action was therefore deemed unnecessary, but there is continued monitoring of surface water, sediments and aquatic organisms at the site (Tab. S1; ADEC_ID_392_1995, ADEC_ID_392_1998, ADEC_ID_392_2018).

Notably the report also states that while there were no acute ecological risks for the source areas around Eielson AFB, there was an exception for SS35 (site 392), where the cumulative ecological risks could lead to reproductive risks to birds and mammals due to exposure to the PCBs and DDT (Tab. S1; ADEC_ID_392_1995). This report also states that all maximum concentrations of the contaminants found in the ground - and surface water exceeds the 'Reasonable Maximum Exposure' by a factor of at least 2. The average values however are below the exposure limit (Tab. S1; ADEC_ID_392_1995).

### Remedial actions in contaminated site clean-up

While these sites pose a large risk for aquatic contaminant mobilisation, remediation efforts have been undertaken at several locations. The military sites in King Salmon are classified as 'Cleanup Complete - Institutional Controls', indicating that they are no longer active and have undergone contaminant removal. The site in Fairbanks remains active as a military base; however, previous assessments by ADEC identified similarly high contamination risks which lead to remedial actions. Ongoing environmental monitoring, including groundwater assessments, has resulted in the removal of over 1000 barrels of contaminants to reduce exposure risks for personnel in the area.

The contaminant database records the status of each CS but does not reflect changes in hazard following remediation. As a result, no clear differences are observed in mean toxicity and solubility between active and cleaned (or institutionally controlled) sites, and their $\Omega$ values remain identical (0.004). This highlights a limitation of the hazard assessment, as reductions in risk due to cleanup are not captured. We therefore excluded the 'Cleaned Up' sites from the risk assessment. The sites that are cleaned up but still under institutional control are included since these sites still contain contaminants and need constant monitoring.

Despite this, a comparison of cleanup status across hazard classes suggests a modest preferential treatment of high-hazard sites. Around 60% of sites classified as 'low' and 'moderate hazard potential' have been cleaned up, compared to 68% of sites with 'high hazard potential'. A chi-square test of independence indicates that these differences are statistically significant. In particular, the difference between 'low' to 'moderate' and 'high' $\Omega$ classes suggests that highly hazardous sites are slightly more likely to be remediated than lower hazard sites (Fisher's exact test with Bonferroni correction: p-value 0.0027).

## Limitations and perspectives for future modelling efforts

While this study provides a first-order spatial assessment of thaw-driven contaminant mobilisation risk, several limitations should be considered.

First of all, the local conditions at the CS can have a major influence on the heat and water exchange between the ground and the atmosphere as well as the subsurface hydrology. As such, the implementation of a Richards equation-based hydrology scheme and lateral subsurface flow into CryoGridLite could lead to more variability of the water table as well as allow for modelled discharge volumes and the possible mobilisation of dissolved toxic substances to be included in the assessment. This does not include any sorption of contaminants to organic matter, which would limit the mobilisation potential.

This research only covers gradual thawing processes and does not include non-gradual thaw processes and its impact on the mobilisation of contaminants under continuous climate change. This includes local and sudden events like forest fires, heat waves, storms, as well as thermokarst and retrogressive thaw slumping.

Abrupt permafrost degradation due to the melting of excess ground ice and the associated formation of thermokarst due to soil subsidence as well as the effects of ponding water at the surface should be investigated [74]. The excess ground ice is also a main limitation for the contaminant mobilisation, where thawing does not lead to deepening of the ALT because melting of ground-ice takes up most of the energy. The added meltwater from this excess ground-ice would also increase the mobilisation if contaminants were present and act as an additional localised water supply.

Furthermore, implementing a vegetation module in the CryoGridLite model would help to accurately reflect the state of permafrost at vegetated sites [97]. Another factor not accounted for in our study is the influence of contaminants on the freezing point depression which should be investigated in future studies.

In addition, the simulations do not account for processes that alter snowpack properties and depth (wind compaction, snow metamorphism, the infiltration and refreezing of meltwater, and snow redistribution due to wind drift). Instead, the model applies a bulk snow density approach to simulate snowpack properties [32]. In addition, water from snowmelt is added to the surface runoff and therefore does not infiltrate into the ground. For example, the storage of toxic liquids in open retention ponds can greatly increase ground heat flux and accelerate permafrost thaw and thermokarst development [98].

Another limitation is related to infrastructure. Industrial facilities and storage tanks in permafrost areas are mostly built on gravel pads, replacing the top organic-rich layer of the soil and increasing the transfer of heat into the ground [99, 100]. The infiltration of rain and meltwater is also slowed down or even prevented by the gravel layer, altering the soil moisture content. Along buildings and gravel embankments snow catch might result in warmer winter ground temperatures [32]. These infrastructure-related influences can accelerate permafrost degradation and destabilize the surrounding soil. Since CS are often found in the vicinity of these infrastructures, they could be affected by such processes, resulting in higher mobilisation potential [5]. To be able to capture these effects, it would be necessary to examine the conditions on-site in detail.

This study offers an initial evaluation of potential environmental impacts, however more comprehensive assessments are required to fully understand the risks associated with thaw-induced mobilisation risk changes and toxicity at high-priority sites.

Therefore, we strongly recommend further investigation into the actual hazard potential of high-priority sites, considering site-specific factors such as local permafrost conditions, contaminant concentrations, and solubility of contaminants. In addition, assessing exposure and the probability of negative effects on human health or the environment from the mobilisation of hazardous substances is critical. Water security has been identified as one of the climate-sensitive health priorities in Canada [101].

# Conclusion

This study provides a first order assessment of the potential mobilisation risk of contaminants stored in permafrost regions in Alaska under current and future permafrost thaw conditions. We evaluate the aquatic hazard potential based on site-specific properties, including toxicity, solubility and proximity to WBs, and combine this with modelled changes in hydrological conditions under climate change to the assess local hydrological mobilisation potential.

Different drivers of the aquatic hazard potential are found across ecoregions. In the Alaska Tundra ecoregion, proximity to water bodies is the dominant factor. Here the extensive wetlands provide efficient pathways for contaminant release and mobilisation, despite the generally lower toxicity (primarily hydrocarbons associated with the Prudhoe Bay oil fields). For the Alaska Boreal Interior and Boreal Cordillera ecoregions higher contaminant toxicity is the main driver of aquatic hazard, reflected by their comparatively drier landscapes with fewer wetlands. This spatial contrast highlights the importance of integrating both chemical properties and landscape characteristics when analysing aquatic impacts.

About 50% of the CS in the Alaska Tundra ecoregion already fall within the ‘high’ to ‘very high’ mobilisation risk categories, increasing to 55% under SSP5-8.5 by the end of this century. In comparison, the Alaska Boreal Interior and Boreal Cordillera ecoregions contain fewer ‘high’ to ‘very high’ risk sites and show limited change under future climate scenarios.

The larger increases in risk in the Alaska Tundra and Brooks Range Tundra ecoregions are driven by larger relative increases in hydrological mobilisation potential $\Phi$, particularly along the northern coastal regions. However, because $\Phi$ remains low in absolute terms, even large relative increases translate into only minor shifts in overall risk classification. Which explains the limited change in aquatic mobilisation risk under future scenarios.

While the northern coastline shows the strongest increase in $\Phi$ under both SSP1-2.6 and SSP5-8.5, this pattern is not reflected in both the WTD and the ALT. Modelled projections indicate widespread drying across central Alaska, south of the Brooks Range. This could contribute to increases in ALT through the loss of latent heat buffering that would otherwise limit permafrost thaw. At the same time, most ecoregions show increased precipitation under future climate scenarios, suggesting that enhanced evapotranspiration, rather than precipitation alone, is the dominant control on future hydrological mobilisation potential.

Since this study only covers a first order assessment of aquatic mobilisation risk, many site-specific processes were not included, such as the absence of cumulative effects of toxicity, non-aqueous liquid phase behaviour of contaminants, colloidal transport, local variations in topography and hydraulic conductivity. Therefore the results presented in this study only serve as a conservative estimate of true mobilisation risk. Including these processes in future studies will improve site-specific risk assessment and provide a better understanding of how permafrost thaw affects contaminant mobilisation.

# Supporting information

**Table S1.** ADEC references of contaminated sites

| REF ID | Source | Document type |
|---|---|---|
| ADEC_ID_706 | `https://dec.alaska.gov/Applications/SPAR/PublicMVC/CSP/Download?documentID=30162&fileName=706_KingSalmonAirStationRapidsCamp.PDF` | Site Summary |
| ADEC_ID_707_2009 | `https://dec.alaska.gov/Applications/SPAR/PublicMVC/CSP/Download?documentID=30161&fileName=707_KingSalmonAirStationRapidsCamp.PDF` | Site Summary |
| ADEC_ID_707_2021 | `https://dec.alaska.gov/Applications/SPAR/PublicMVC/CSP/Download?documentID=56000&fileName=707_FINAL%202020%20KSD%20RAO%20LUC%20%281%29.pdf` | Remedial Action Operations & Land Use Control Inspections |
| ADEC_ID_392_1995 | `https://dec.alaska.gov/Applications/SPAR/PublicMVC/CSP/Download?documentID=56819&fileName=392_OU3%2C4%2C5%20ROD%201995.pdf` | Record of Decision |
| ADEC_ID_392_1998 | `https://dec.alaska.gov/Applications/SPAR/PublicMVC/CSP/Download?documentID=56820&fileName=392_OU3%2C4%2C5%20ROD%20Amendment%201998.pdf` | Declaration of the Amended Record of Decision |
| ADEC_ID_392_2018 | `https://dec.alaska.gov/Applications/SPAR/PublicMVC/CSP/Download?documentID=31174&fileName=392_2018.08.01%20Final%20RI%20FS%20ManagementPlan%20SS035.pdf` | Installation Restoration Program |

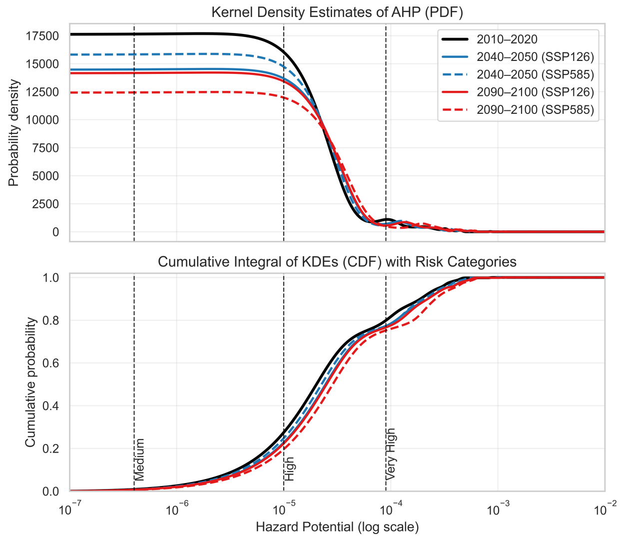


**Fig S2. probability density function of mobilisation risk for both climate scenarios** for mid century and end of century simulations, including the current conditions. Vertical dotted lines show the binning for the risk categories. Due to climate change the 'high risk' bin shows a change toward the 'very high risk' bin. This is accompanied by a lowering of lower risk sites. b) Cumulative density function of mobilisation risk. Under the SSP5-8.5 scenario there is a shift toward higher probabilities for increases in mobilisation risk. At the same cumulative probability, the curves for end of century scenarios show higher categorisation.

## S3

**Model evaluation** The model performance was evaluated at six sites across Alaska (see Fig. 1) using observations of active layer thicknesses, ground temperatures, and water table depths. For five out of the six sites, the measured ALT was within the range of the simulated ensemble of ALTs (Fig. S3.1), with the best agreements for the northernmost sites. For one site (Wickersham) which is located in central Alaska within the zone of discontinuous permafrost, the simulated ALTs were substantially larger (about 1 to 1.5 m) than the observations (around 0.5 m). This can be explained by site-specific conditions (high elevation, vegetation cover) not captured by the model ensemble. Simulated ground temperatures agree well with observations for the site Utqiagvik (Barrow), despite an overestimation of the annual temperature amplitude in a depth of 2m. Likely, this can be attributed to differences in the ground stratigraphy (ice content) between the observations and simulations, suggesting that the model ensemble does not capture the full range of environmental conditions. Finally, the comparison of water table depths for the site Utqiagvik revealed that while the ensemble of simulations captures the observed range of WTs well, individual simulations show a much lower intra-annual variability than suggested by the observations. However, the model evaluation overall suggests that CryoGridLite is capable of simulating the ground thermal and hydrological regimes well, in particular on annual-to-decadal timescales, which has also been shown by Langer et al [74].

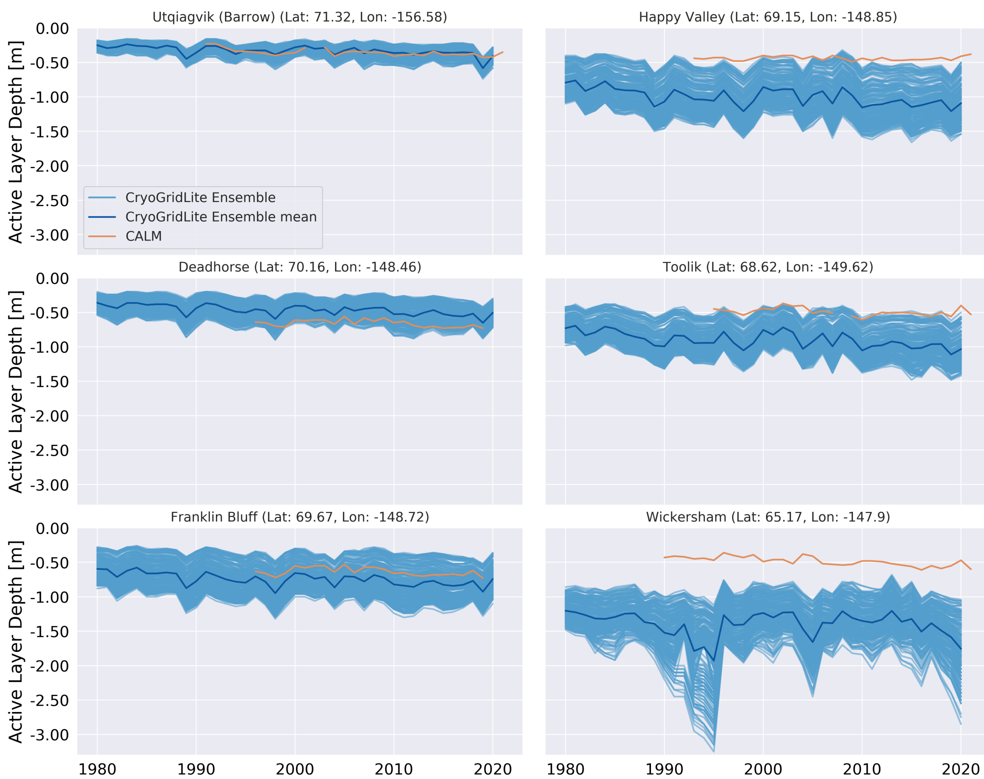


**Fig S3.1. Measured (orange) and simulated (blue) maximum annual active layer depth for the period from 1980 to 2020 at the six validation sites.** The ensemble mean at each of the sites is shown in dark blue. The subplots of the validation sites are sorted according to their geographical location from north (upper left) to south (lower right).

The comparison of simulated ALT from the ensemble runs with the CALM measurements shows that the maximum annual thaw depths at the three northernmost validation sites (Utqiagvik, Deadhorse and Franklin Bluff) fall within the ensemble range throughout the entire validation period (Fig. S3.2). At Happy Valley and Toolik, the measured ALT values lie at the upper end of the ensemble range, with the measured ALT at Happy Valley being 5 - 10cm lower than the minimum ensemble ALT in most years. At the southernmost validation site, Wickersham, simulated ALT values are on average approximately 0.75m larger than the measured values. Fig. S3.2 further shows that the ensemble range shifts toward larger ALT values with decreasing latitude. In contrast, observations indicate maximum annual thaw depths of approximately 0.5m at Toolik and Wickersham, while at Deadhorse, further north, ALT is approximately 0.65m. The simulations capture inter-annual variability reasonably well at Utqiagvik and Franklin Bluff, but do not reproduce it adequately at Wickersham. Notably, some ensemble members exhibit unusually strong variability around 1994 and 1995. With the exception of Deadhorse, the model setup used in this study generally tends to overestimate ALT.

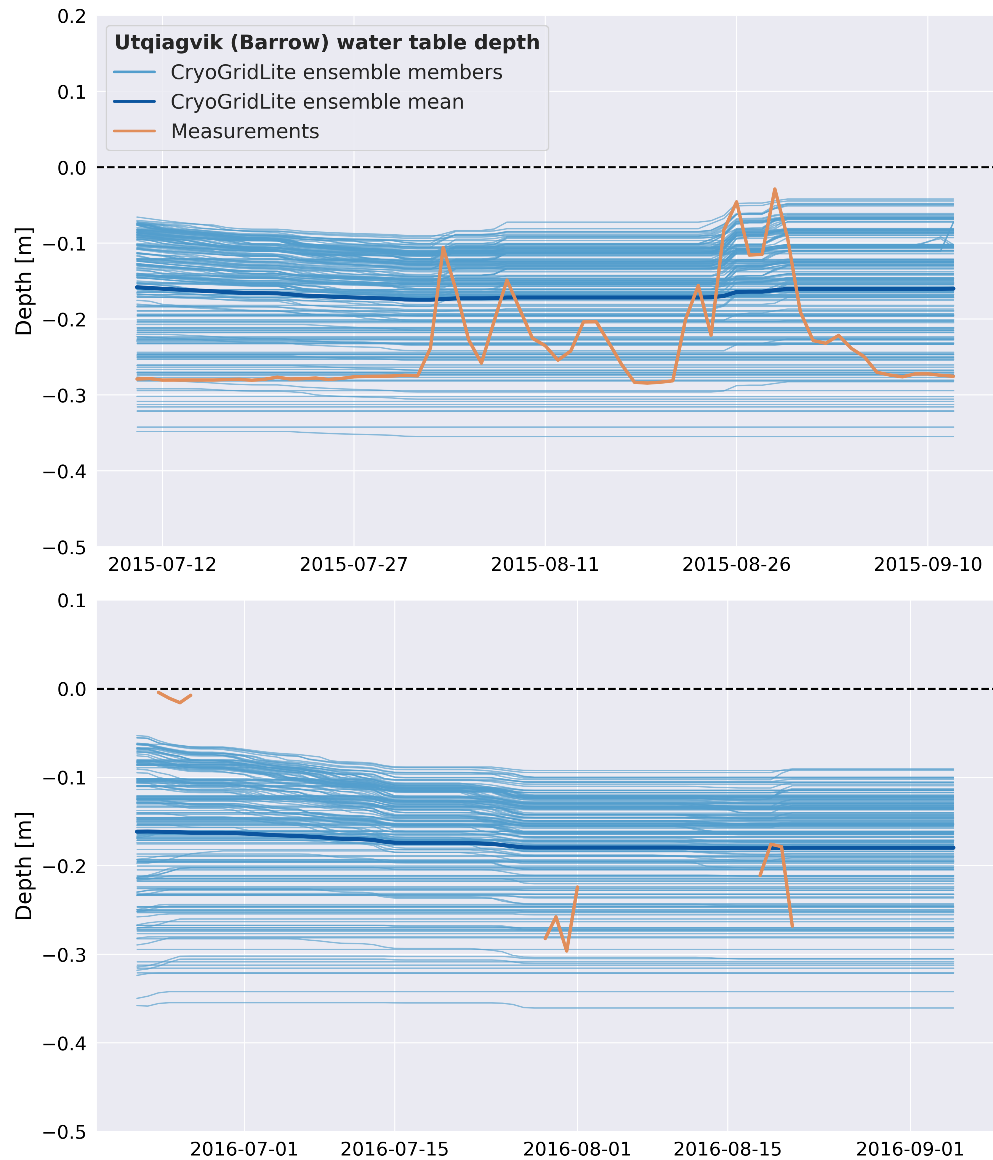


**Fig S3.2. Measured (orange) and simulated (blue) maximum daily water table depth (WTD) for the summers of 2015 (top) and 2016 (bottom) at Utqiagvik (Barrow)**. The dotted black line indicates the ground surface. The significant data gaps in 2016 result from discontinuous measurements of the water table that year.

Due to the limited availability of validation data, comparison of ensemble-simulated water table depth (WTD) was only possible for the Utqiagvik site. As shown in Fig. S3.2, the measured summer WTD during

2015 and 2016 was almost always within the ensemble range. Observations exceeded the ensemble range only during a peak in late August 2015 and at the beginning of the thaw period in June 2016. However, the simulations did not reproduce the observed intra-seasonal variability of the water table. Comparison of the ensemble mean WTD with observations shows that the simulated water table at Utqiagvik was, on average, approximately 5 - 10 cm too high.

**Model sensitivity** The sensitivity analysis at the Utqiagvik site shows that the difference between the ALT and the water table, corresponding to the thickness of the fully saturated portion of the active layer, is largely controlled by the volumetric soil organic carbon (VSOC) content in the upper 0.3 m of the soil (Fig. S3.3). The coefficient of determination (R2 $\sim$ 0.9) indicates a very strong negative correlation between the VSOC and the ALT - water table difference. A doubling of the VSOC results in a reduction of more than 30% in the thickness of the fully saturated thawed soil layer. The Field Capacity Factor (FCF) shows the second highest correlation, with an R2 value of 0.032, approximately two orders of magnitude smaller than that of VSOC. No significant correlations were found between the thickness of the fully saturated portion of the Active Layer and any other parameters (Fig. S3.3)

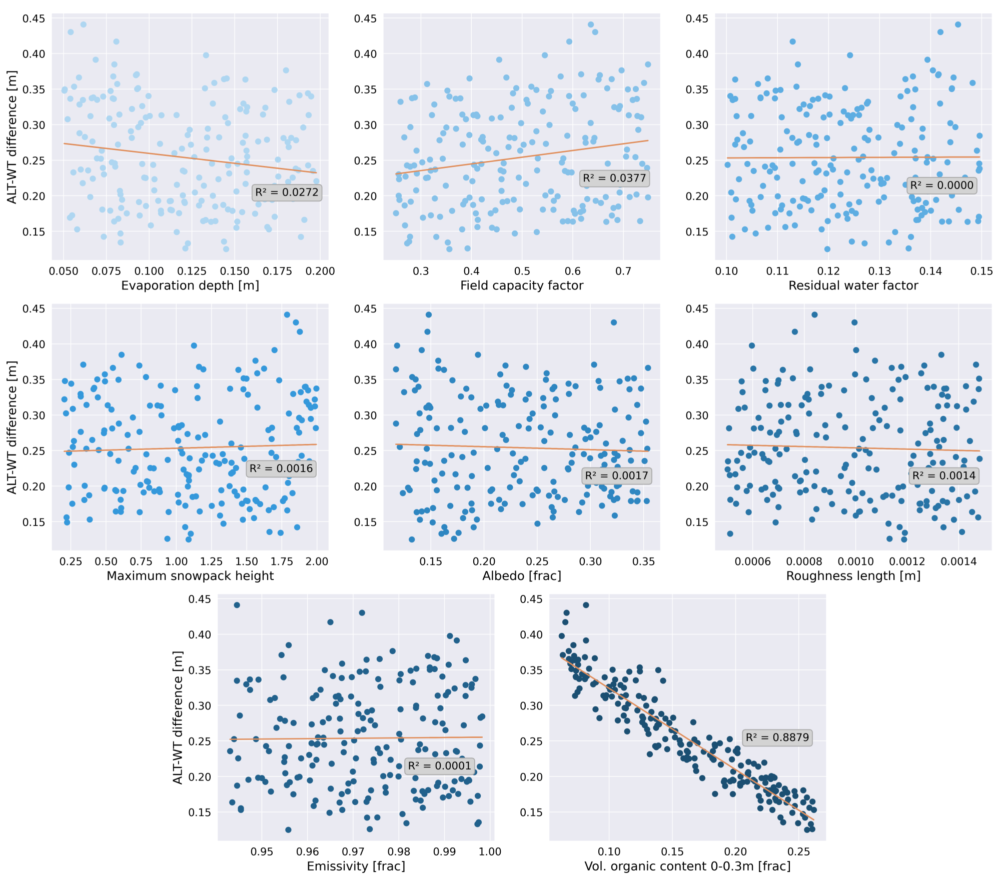


**Fig S3.3. Correlations between the eight parameters that were varied in the ensemble simulations for the model validation at the Utqiagvik (Barrow) site** and the active layer thickness (ALT) - water table (WT) difference in eight separate scatter plots. The linear regression models are shown as orange lines and the coefficient of determination (R2) is displayed for each variable.

## Acknowledgments

DK acknowledges the POLMAR Graduate School and the SENSE Research School for providing an interdisciplinary research and training environment that supported this work. We further acknowledge the providers of the openly available datasets and model products used in this study.

## References

1. Anisimov OA, Nelson FE. Permafrost distribution in the Northern Hemisphere under scenarios of climatic change. Global and Planetary Change. 1996 Aug;14(1–2):59–72. Available from: https://doi.org/10.1016/0921-8181(96)00002-1. doi:10.1016/0921-8181(96)00002-1.

2. Jorgenson MT, Shur YL, Pullman ER. Abrupt increase in permafrost degradation in Arctic Alaska. Geophysical Research Letters. 2006 Jan;33(2). Available from: https://doi.org/10.1029/2005gl024960. doi:10.1029/2005gl024960.

3. Liljedahl AK, Boike J, Daanen RP, Fedorov AN, Frost GV, Grosse G, et al. Pan-Arctic ice-wedge degradation in warming permafrost and its influence on tundra hydrology. Nature Geoscience. 2016;9(4):312–318. doi:10.1038/ngeo2674.

4. Liljedahl AK, Witharana C, Manos E. The capillaries of the Arctic tundra. Nature Water. 2024 Jul;2(7):611–614. Available from: https://doi.org/10.1038/s44221-024-00276-9. doi:10.1038/s44221-024-00276-9.

5. Langer M, Von Deimling TS, Westermann S, Rolph R, Rutte R, Antonova S, et al. Thawing permafrost poses environmental threat to thousands of sites with legacy industrial contamination. Nature Communications. 2023 mar;14(1). Available from: https://doi.org/10.1038/s41467-023-37276-4. doi:10.1038/s41467-023-37276-4.

6. Dyke LD. Contaminant migration through the permafrost active layer, Mackenzie Delta area, Northwest Territories, Canada. Polar Record. 2001;37(202):215-28.

7. Abou-Sayed A, Andrews D, Buhidma I. Evaluation of oily waste injection below the permafrost in Prudhoe Bay field. In: SPE California Regional Meeting. OnePetro; 1989. .

8. Ayele Y, Barabadi A, Barabady J. Drilling waste handling and management in the High North. In: 2013 IEEE International Conference on Industrial Engineering and Engineering Management. IEEE; 2013. p. 673-8.

9. Romanovsky VE, Smith SL, Christiansen HH. Permafrost thermal state in the polar Northern Hemisphere during the international polar year 2007–2009: a synthesis. Permafrost and Periglacial processes. 2010;21(2):106-16.

10. Kokelj SV, Jorgenson MT. Advances in thermokarst research. Permafrost and Periglacial Processes. 2013;24(2):108-19. Available from: https://doi.org/10.1002/ppp.1779. doi:10.1002/ppp.1779.

11. Walvoord MA, Kurylyk BL. Hydrologic Impacts of Thawing Permafrost—A Review. Vadose Zone Journal. 2016 Jun;15(6):1–20. Available from: https://doi.org/10.2136/vzj2016.01.0010. doi:10.2136/vzj2016.01.0010.

12. Farquharson LM, Romanovsky VE, Cable WL, Walker DA, Kokelj SV, Nicolsky D. Climate change drives widespread and rapid thermokarst development in very cold permafrost in the Canadian High Arctic. Geophysical Research Letters. 2019 Jun;46(12):6681–6689. Available from: https://doi.org/10.1029/2019gl082187. doi:10.1029/2019gl082187.

13. Biskaborn BK, Smith SL, Noetzli J, Matthes H, Vieira G, Streletskiy DA, et al. Permafrost is warming at a global scale. Nature communications. 2019;10(1):1-11.

14. Smith LC, Sheng Y, MacDonald GM, Hinzman LD. Disappearing Arctic lakes. Science. 2005 Jun;308(5727):1429. Available from: https://doi.org/10.1126/science.1108142. doi:10.1126/science.1108142.

15. Nitze I, Cooley SW, Duguay CR, Jones BM, Grosse G. The catastrophic thermokarst lake drainage events of 2018 in northwestern Alaska: fast-forward into the future. The Cryosphere. 2020;14(12):4279-97.

16. Bintanja R. The impact of Arctic warming on increased rainfall. Scientific Reports. 2018 Oct;8(1):16001. Available from: https://doi.org/10.1038/s41598-018-34450-3. doi:10.1038/s41598-018-34450-3.

17. Arp CD, Whitman MS, Kemnitz R, Stuefer SL. Evidence of hydrological intensification and regime change from Northern Alaskan Watershed runoff. Geophysical Research Letters. 2020 Aug;47(17). Available from: https://doi.org/10.1029/2020gl089186. doi:10.1029/2020gl089186.

18. Beel CR, Heslop JK, Orwin JF, Pope MA, Schevers AJ, Hung JKY, et al. Emerging dominance of summer rainfall driving High Arctic terrestrial-aquatic connectivity. Nature Communications. 2021 Mar;12(1):1448. Available from: https://www.nature.com/articles/s41467-021-21759-3. doi:10.1038/s41467-021-21759-3.

19. Pringle C. The need for a more predictive understanding of hydrologic connectivity. Aquatic Conservation Marine and Freshwater Ecosystems. 2003 Oct;13(6):467–471. Available from: https://doi.org/10.1002/aqc.603. doi:10.1002/aqc.603.

20. Adams EM, Von Hippel FA, Hungate BA, Buck CL. Polychlorinated biphenyl (PCB) contamination of subsistence species on Unalaska Island in the Aleutian Archipelago. Heliyon. 2019 Dec;5(12):e02989. Available from: https://doi.org/10.1016/j.heliyon.2019.e02989. doi:10.1016/j.heliyon.2019.e02989.

21. Scrudato RJ, Chiarenzelli JR, Miller PK, Alexander CR, Arnason J, Zamzow K, et al. Contaminants at Arctic formerly used defense sites. Journal of Local and Global Health Science. 2012 Nov;2012(1). Available from: https://doi.org/10.5339/jlghs.2012.2. doi:10.5339/jlghs.2012.2.

22. AMAP. AMAP Assessment 2016: Chemical of Emerging Arctic Concern. ISBN – 978-82-7971-104-9. Oslo, Norway; 2017. Available from: https://www.amap.no/documents/download/3003/inline.

23. Khamkhash A, Srivastava V, Ghosh T, Akdogan G, Ganguli R, Aggarwal S. Mining-Related selenium contamination in Alaska, and the state of current knowledge. Minerals. 2017 Mar;7(3):46. Available from: https://doi.org/10.3390/min7030046. doi:10.3390/min7030046.

24. Wagner AM, Barker AJ. Distribution of polycyclic aromatic hydrocarbons (PAHs) from legacy spills at an Alaskan Arctic site underlain by permafrost. Cold Regions Science and Technology. 2018 Nov;158:154–165. Available from: https://doi.org/10.1016/j.coldregions.2018.11.012. doi:10.1016/j.coldregions.2018.11.012.

25. Bartsch A, Pointner G, Nitze I, Efimova A, Jakober D, Ley S, et al. Expanding infrastructure and growing anthropogenic impacts along Arctic coasts. Environmental Research Letters. 2021 Oct;16(11):115013. Available from: https://doi.org/10.1088/1748-9326/ac3176. doi:10.1088/1748-9326/ac3176.

26. Muir D, Gunnarsdóttir MJ, Koziol K, von Hippel FA, Szumińska D, Ademollo N, et al. Local sources versus long-range transport of organic contaminants in the Arctic: future developments related to climate change. Environmental Science Advances. 2025 Jan;4:355-408. Available from: http://dx.doi.org/10.1039/D4VA00240G. doi:10.1039/D4VA00240G.

27. Mohammed AA, Bense VF, Kurylyk BL, Jamieson RC, Johnston LH, Jackson AJ. Modeling Reactive Solute Transport in Permafrost-Affected Groundwater Systems. Water Resources Research. 2021;57(7). doi:10.1029/2020wr028771.

28. McGovern M, Borgå K, Heimstad E, Ruus A, Christensen G, Evenset A. Small Arctic rivers transport legacy contaminants from thawing catchments to coastal areas in Kongsfjorden, Svalbard. Environmental Pollution. 2022;304:119191. doi:10.1016/j.envpol.2022.119191.

29. MacInnis J, De Silva AO, Lehnherr I, Muir DCG, St Pierre KA, St Louis VL, et al. Investigation of perfluoroalkyl substances in proglacial rivers and permafrost seep in a high Arctic watershed. Environmental Science: Processes amp; Impacts. 2022;24(1):42–51. doi:10.1039/d1em00349f.

30. Hjort J, Karjalainen O, Aalto J, Westermann S, Romanovsky VE, Nelson FE, et al. Degrading permafrost puts Arctic infrastructure at risk by mid-century. Nature communications. 2018;9(1):1-9.

31. Karjalainen O, Aalto J, Luoto M, Westermann S, Romanovsky VE, Nelson FE, et al. Circumpolar permafrost maps and geohazard indices for near-future infrastructure risk assessments. Scientific data. 2019;6(1):1-16.

32. Schneider von Deimling T, Lee H, Ingeman-Nielsen T, Westermann S, Romanovsky V, Lamoureux S, et al. Consequences of permafrost degradation for Arctic infrastructure – bridging the model gap between regional and engineering scales. The Cryosphere. 2021;15(5):2451-71. Available from: https://tc.copernicus.org/articles/15/2451/2021/. doi:10.5194/tc-15-2451-2021.

33. Ni J, Wu T, Zhu X, Wu X, Pang Q, Zou D, et al. Risk assessment of potential thaw settlement hazard in the permafrost regions of Qinghai-Tibet Plateau. Science of The Total Environment. 2021;776:145855. Available from: https://www.sciencedirect.com/science/article/pii/S0048969721009220. doi:https://doi.org/10.1016/j.scitotenv.2021.145855.

34. Duvillard PA, Ravanel L, Schoeneich P, Deline P, Marcer M, Magnin F. Qualitative risk assessment and strategies for infrastructure on permafrost in the French Alps. Cold Regions Science and Technology. 2021;189:103311.

35. Zhang S, Niu F, Wang S, Sun Y, Wang J, Dong T. Risk assessment of engineering diseases of embankment–bridge transition section for railway in permafrost regions. Permafrost and Periglacial Processes. 2022;33(1):46-62.

36. Ramage J, Jungsberg L, Wang S, Westermann S, Lantuit H, Heleniak T. Population living on permafrost in the Arctic. Population and Environment. 2021 Jan;43(1):22–38. Available from: https://doi.org/10.1007/s11111-020-00370-6. doi:10.1007/s11111-020-00370-6.

37. [ICC] ICCA. Alaskan Inuit Food Security Conceptual Framework: How to assess the Arctic from an Inuit perspective. Anchorage, Alaska; 2015. Available from: https://iccalaska.org/wp-icc/wp-content/uploads/2016/05/Food-Security-Full-Technical-Report.pdf.

38. AP. Alaska closes 2 lakes to fishing after finding contamination. https://apnewscom. 2019 apr. Available from: https://apnews.com/article/36b8705c6fb74bec996a6198231959ad.

39. O'Donnell JA, Carey MP, Koch JC, Baughman C, Hill K, Zimmerman CE, et al. Metal mobilization from thawing permafrost to aquatic ecosystems is driving rusting of Arctic streams. Communications Earth Environment. 2024 May;5(1). Available from: https://doi.org/10.1038/s43247-024-01446-z. doi:10.1038/s43247-024-01446-z.

40. Stribling SA, Lamontagne-Hallé P, Hemmings D, MacNeil T, McKenzie JM. Quantifying Changing Groundwater Exfiltration at a High Arctic Site due to Climate Change. Hydrological Processes. 2025 Aug;39(8):e70243. Available from: https://doi.org/10.1002/hyp.70243. doi:10.1002/hyp.70243.

41. Bogdanova E, Lobanov A, Andronov SV, Soromotin A, Popov A, Skalny AV, et al. Challenges of changing water sources for human wellbeing in the Arctic zone of Western Siberia. Water. 2023 Apr;15(8):1577. Available from: https://doi.org/10.3390/w15081577. doi:10.3390/w15081577.

42. Shulski M, Wendler G. The climate of Alaska. Fairbanks, Alaska, United States of America: University of Alaska Press; 2007. Available from: https://books.google.nl/books?hl=nl&lr=&id=aUDWK8zDr50C&oi=fnd&pg=PR7&dq=Alaska+climate+&ots=8j3X4r6Vt7&sig=ifHILYKBfxWRSeg107wam1oowq4&redir_esc=y#v=onepage&q=Alaska%20climate&f=false.

43. Wiken E, Jiménez Nava F, Griffith G. North American Terrestrial Ecoregions - Level III. Montreal, Canada; 2011. Available from: https://dmap-prod-oms-edc.s3.us-east-1.amazonaws.com/ORD/Ecoregions/pubs/NA_TerrestrialEcoregionsLevel3_Final-2june11_CEC.pdf.

44. Obu J, Westermann S, Bartsch A, Berdnikov N, Christiansen HH, Dashtseren A, et al. Northern Hemisphere permafrost map based on TTOP modelling for 2000–2016 at 1 km2 scale. Earth-Science Reviews. 2019;193:299-316.

45. for Environmental Cooperation (CEC) C. North American Envirnmental Atlas - Terrestrial Ecoregions: Level II; 2021. Available from: https://www.epa.gov/eco-research/ecoregions-north-america.

46. Walsh JE, Brettschneider B. Attribution of recent warming in Alaska. Polar Science. 2019 Sep;21:101–109. Available from: https://doi.org/10.1016/j.polar.2018.09.002. doi:10.1016/j.polar.2018.09.002.

47. EPA U. Climate Change Indicators: Permafrost; 2021. Accessed: 2022-08-16. https://www.epa.gov/climate-indicators/climate-change-indicators-permafrost#ref7.

48. Smith SL, O'Neill HB, Isaksen K, Noetzli J, Romanovsky VE. The changing thermal state of permafrost. Nature Reviews Earth amp; Environment. 2022 Jan;3(1):10–23. doi:10.1038/s43017-021-00240-1.

49. Farquharson LM, Romanovsky VE, Kholodov A, Nicolsky D. Sub-aerial talik formation observed across the discontinuous permafrost zone of Alaska. Nature Geoscience. 2022 Jun;15:475-81.

50. ADEC. Alaska Dept. of Environmental Conservation [ADEC] — The Contaminated Sites Program;. Available from: https://dec.alaska.gov/spar/csp/.

51. Kaiser S, Boike J, Grosse G, Langer M. Multisource synthesized inventory of CRitical infrastructure and HUman-Impacted areas in AlaSka (SIRIUS). Earth System Science Data. 2024 Aug;16(8):3719–3753. Available from: https://doi.org/10.5194/essd-16-3719-2024. doi:10.5194/essd-16-3719-2024.

52. Messager ML, Lehner B, Grill G, Nedeva I, Schmitt O. Estimating the volume and age of water stored in global lakes using a geo-statistical approach. Nature communications. 2016;7(1):1-11.

53. Allen GH, Pavelsky TM. Global extent of rivers and streams. Science. 2018;361(6402):585-8.

54. Pekel JF, Cottam A, Gorelick N, Belward AS. High-resolution mapping of global surface water and its long-term changes. Nature. 2016;540(7633):418-22.

55. of Solid Waste UEO, Response E. Using Toxicity Tests in Ecological Risk Assessment. ECO Update. 1994 Mar;2(19345.0–05I). Available from: https://www.epa.gov/sites/default/files/2015-09/documents/v2no1.pdf.

56. für Arbeitsschutz der DGUV I GESTIS substance Database;. Available from: https://gestis-database.dguv.de.

57. Kim S, Chen J, Cheng T, Gindulyte A, He J, He S, et al. PubChem 2025 update. Nucleic Acids Research. 2024 Nov;53(D1):D1516–D1525. Available from: https://doi.org/10.1093/nar/gkae1059. doi:10.1093/nar/gkae1059.

58. of Federal Regulations C. 40 CFR 156.62 Toxicity Category.; 2025. Available from: https://www.ecfr.gov/current/title-40/chapter-I/subchapter-E/part-156/subpart-D/section-156.62.

59. [ILO] ILO. International Chemical Safety Cards;. Available from: https://chemicalsafety.ilo.org/dyn/icsc/showcard.home.

60. Porter C, Morin P, Howat I, Noh MJ, Bates B, Peterman K, et al.. ArcticDEM, Version 3. Harvard Dataverse; 2018. Available from: https://doi.org/10.7910/DVN/OHHUKH. doi:10.7910/DVN/OHHUKH.

61. O'Callaghan JF, Mark DM. The extraction of drainage networks from digital elevation data. Computer Vision, Graphics, and Image Processing. 1984;28(3):323-44. Available from: https://www.sciencedirect.com/science/article/pii/S0734189X84800110. doi:https://doi.org/10.1016/S0734-189X(84)80011-0.

62. Barnes R. RichDEM: Terrain Analysis Software; 2016. Available from: http://github.com/r-barnes/richdem.

63. Hersbach H, Bell B, Berrisford P, Hirahara S, Horányi A, Muñoz-Sabater J, et al. The ERA5 global reanalysis. Quarterly Journal of the Royal Meteorological Society. 2020;146(730):1999-2049.

64. Müller WA, Jungclaus JH, Mauritsen T, Baehr J, Bittner M, Budich R, et al. A higher-resolution version of the max planck institute earth system model (MPI-ESM1. 2-HR). Journal of Advances in Modeling Earth Systems. 2018;10(7):1383-413.

65. Copernicus Climate Change Service. CMIP6 Climate Projections. Copernicus Climate Change Service (C3S) Climate Data Store (CDS); 2021. Accessed on 01-2021. Available from: https://doi.org/10.24381/cds.c866074c. doi:10.24381/cds.c866074c.

66. Koven CD, Schuur E, Schädel C, Bohn T, Burke E, Chen G, et al. A simplified, data-constrained approach to estimate the permafrost carbon–climate feedback. Philosophical Transactions of the Royal Society A: Mathematical, Physical and Engineering Sciences. 2015;373(2054):20140423.

67. Faroux S, Kaptué Tchuenté A, Roujean JL, Masson V, Martin E, Le Moigne P. ECOCLIMAP-II/Europe: A twofold database of ecosystems and surface parameters at 1 km resolution based on satellite information for use in land surface, meteorological and climate models. Geoscientific Model Development. 2013;6(2):563-82.

68. Masson V, Champeaux JL, Chauvin F, Meriguet C, Lacaze R. A global database of land surface parameters at 1-km resolution in meteorological and climate models. Journal of climate. 2003;16(9):1261-82.

69. Hugelius G, Tarnocai C, Broll G, Canadell J, Kuhry P, Swanson D. The Northern Circumpolar Soil Carbon Database: spatially distributed datasets of soil coverage and soil carbon storage in the northern permafrost regions. Earth System Science Data. 2013;5(1):3-13.

70. Pelletier JD, Broxton PD, Hazenberg P, Zeng X, Troch PA, Niu GY, et al. A gridded global data set of soil, intact regolith, and sedimentary deposit thicknesses for regional and global land surface modeling. Journal of Advances in Modeling Earth Systems. 2016;8(1):41-65.

71. Westermann S, Langer M, Boike J, Heikenfeld M, Peter M, Etzelmüller B, et al. Simulating the thermal regime and thaw processes of ice-rich permafrost ground with the land-surface model CryoGrid 3. Geoscientific Model Development. 2016;9(2):523-46.

72. Clapp RB, Hornberger GM. Empirical equations for some soil hydraulic properties. Water resources research. 1978;14(4):601-4.

73. Le Moigne P, Boone A, Calvet J, Decharme B, Faroux S, Gibelin A, et al. SURFEX scientific documentation. Note de centre (CNRM/GMME), Météo-France, Toulouse, France. 2009;268.

74. Langer M, Nitzbon J, Groenke B, Assmann LM, Von Deimling TS, Stuenzi SM, et al. The evolution of Arctic permafrost over the last 3 centuries from ensemble simulations with the CryoGridLite permafrost model. the Cryosphere. 2024 Jan;18(1):363–385. Available from: https://doi.org/10.5194/tc-18-363-2024. doi:10.5194/tc-18-363-2024.

75. Nitzbon J, Krinner G, Von Deimling TS, Werner M, Langer M. First quantification of the permafrost heat sink in the Earth's climate system. Geophysical Research Letters. 2023 Jun;50(12). Available from: https://doi.org/10.1029/2022gl102053. doi:10.1029/2022gl102053.

76. Chen R, Nitzbon J, Von Deimling TS, Stuenzi SM, Chan NH, Boike J, et al. Potential vegetation greenness changes in the permafrost areas over the Tibetan Plateau under future climate warming. Global and Planetary Change. 2025 Apr;252:104833. Available from: https://doi.org/10.1016/j.gloplacha.2025.104833. doi:10.1016/j.gloplacha.2025.104833.

77. Das NN, Mohanty BP. Root zone soil moisture assessment using remote sensing and vadose zone modeling. Vadose Zone Journal. 2006;5(1):296-307.

78. Carsel RF, Parrish RS. Developing joint probability distributions of soil water retention characteristics. Water resources research. 1988;24(5):755-69.

79. Benson D, Wheatcraft S, Meerschaert M. Application of a fractional advection-dispersionequation. Water Resources Research. 2000 Jun;36(6):1403–1412. Available from: https://agupubs-onlinelibrary-wiley-com.vu-nl.idm.oclc.org/doi/epdf/10.1029/2000WR900031.

80. De Jonge LW, Kjaergaard C, Moldrup P. Colloids and Colloid-Facilitated Transport of Contaminants in soils: an Introduction. Vadose Zone Journal. 2004 May;3(2):321–325. Available from: https://doi.org/10.2113/3.2.321. doi:10.2113/3.2.321.

81. Ukalska-Jaruga A, Bejger R, Smreczak B, Podlasiński M. Sorption of Organic Contaminants by Stable Organic Matter Fraction in Soil. Molecules. 2023 Jan;28(1):429. Available from: https://doi.org/10.3390/molecules28010429. doi:10.3390/molecules28010429.

82. Nowacki GJ, Spencer P, Fleming M, Brock T, Jorgenson T. Unified Ecoregions of Alaska: 2001. Antarctica a Keystone in a Changing World. 2003 Jan. Available from: https://doi.org/10.3133/ofr2002297. doi:10.3133/ofr2002297.

83. Mueller R, Yingling V. Environmental fate and transport for per- and polyfluoroalkyl substances. Washington DC, United States of America; 2018. Available from: https://www.nccoast.org/wp-content/uploads/2018/10/ITRC-PFAS-Transport-Fact-Sheet.pdf.

84. Hasan MM, Habib A, Alam MJ, Islam S, Halim E. Industrial Applications, Environmental Fate, Human Exposure, and Health Effects of PFAS. Pollutants. 2025;5(4):43. Available from: https://doi.org/10.3390/pollutants5040043. doi:10.3390/pollutants5040043.

85. Cousins IT, DeWitt JC, Glüge J, Goldenman G, Herzke D, Lohmann R, et al. The high persistence of PFAS is sufficient for their management as a chemical class. Environmental Science Processes Impacts. 2020 Jan;22(12):2307–2312. Available from: https://doi.org/10.1039/d0em00355g. doi:10.1039/d0em00355g.

86. Yi Y, Kimball JS, Chen RH, Moghaddam M, Reichle RH, Mishra U, et al. Characterizing permafrost active layer dynamics and sensitivity to landscape spatial heterogeneity in Alaska. the Cryosphere. 2018 Jan;12(1):145–161. Available from: https://doi.org/10.5194/tc-12-145-2018. doi:10.5194/tc-12-145-2018.

87. Ballinger TJ, Bhatt US, Bieniek PA, Brettschneider B, Lader RT, Littell JS, et al. Alaska Terrestrial and Marine Climate Trends, 1957–2021. Journal of Climate. 2023 Mar;36(13):4375–4391. Available from: https://doi.org/10.1175/jcli-d-22-0434.1. doi:10.1175/jcli-d-22-0434.1.

88. Clayton LK, Schaefer K, Battaglia MJ, Bourgeau-Chavez L, Chen J, Chen RH, et al. Active layer thickness as a function of soil water content. Environmental Research Letters. 2021 Apr;16(5):055028. Available from: https://doi.org/10.1088/1748-9326/abfa4c. doi:10.1088/1748-9326/abfa4c.

89. Thunberg SM, Walsh JE, Euskirchen ES, Redilla K, Rocha AV. Surface moisture budget of tundra and boreal ecosystems in Alaska: Variations and drivers. Polar Science. 2021 May;29:100685. Available from: https://doi.org/10.1016/j.polar.2021.100685. doi:10.1016/j.polar.2021.100685.

90. Bintanja R, Selten FM. Future increases in Arctic precipitation linked to local evaporation and sea-ice retreat. Nature. 2014 May;509(7501):479–482. Available from: https://doi.org/10.1038/nature13259. doi:10.1038/nature13259.

91. Bring A, Fedorova I, Dibike Y, Hinzman L, Mård J, Mernild SH, et al. Arctic terrestrial hydrology: A synthesis of processes, regional effects, and research challenges. Journal of Geophysical Research Biogeosciences. 2016 Feb;121(3):621–649. Available from: https://doi.org/10.1002/2015jg003131. doi:10.1002/2015jg003131.

92. Hjort J, Streletskiy D, Doré G, Wu Q, Bjella K, Luoto M. Impacts of permafrost degradation on infrastructure. Nature Reviews Earth & Environment. 2022;3(1):24-38.

93. Tebaldi C, Debeire K, Eyring V, Fischer E, Fyfe J, Friedlingstein P, et al. Climate model projections from the Scenario Model Intercomparison Project (ScenarioMIP) of CMIP6. Earth System Dynamics. 2021 03;12:253-93. doi:10.5194/esd-12-253-2021.

94. Anisimov O, Reneva S. Permafrost and changing climate: the Russian perspective. AMBIO: A Journal of the Human Environment. 2006 Jun;35(4):169–175. doi:10.1579/0044-7447(2006)35.

95. Nelson FE, Anisimov OA, Shiklomanov NI. Subsidence risk from thawing permafrost. Nature. 2001 Apr;410(6831):889–890. Available from: https://doi.org/10.1038/35073746. doi:0.1038/35073746.

96. Brown J, Ferrians O, Heginbottom J, Melnikov ES. Circum-Arctic Map of Permafrost and Ground-Ice Conditions, Version 2 [Data set]. NASA National Snow and Ice Data Center, Distributed Active Archive Center; 2002. Available from: https://doi.org/10.7265/skbg-kf16. doi:10.7265/skbg-kf16.

97. Stuenzi SM, Boike J, Cable W, Herzschuh U, Kruse S, Pestryakova LA, et al. Variability of the surface energy balance in permafrost-underlain boreal forest. Biogeosciences. 2021;18(2):343-65. Available from: https://bg.copernicus.org/articles/18/343/2021/. doi:10.5194/bg-18-343-2021.

98. Langer M, Westermann S, Boike J, Kirillin G, Grosse G, Peng S, et al. Rapid degradation of permafrost underneath waterbodies in tundra landscapes—toward a representation of thermokarst in land surface models. Journal of Geophysical Research: Earth Surface. 2016;121(12):2446-70.

99. Ferrians OJ, Kachadoorian R, Greene GW. Permafrost and related engineering problems in Alaska. USGS Professional Paper. 1969 Jan. Available from: https://doi.org/10.3133/pp678. doi:10.3133/pp678.

100. Walker WS, Gorelik SR, Cook-Patton SC, Baccini A, Farina MK, Solvik KK, et al. The global potential for increased storage of carbon on land. Proceedings of the National Academy of Sciences. 2022 May;119(23). Available from: https://doi.org/10.1073/pnas.2111312119. doi:10.1073/pnas.2111312119.

101. Harper SL, Edge VL, Ford J, Willox AC, Wood M, McEwen SA. Climate-sensitive health priorities in Nunatsiavut, Canada. BMC Public Health. 2015 Jul;15(1). Available from: https://doi.org/10.1186/s12889-015-1874-3. doi:10.1186/s12889-015-1874-3.